Progress Report

OWEB Grant 208-8002-5776

By

John Selker

December 30, 2009

Department of Biological & Ecological Engineering
rm 210 Gilmore Hall
Oregon State University
Corvallis, Oregon 97331-3906
tel: +1-541-737-6304
fax: +1-541-737-2082
John.Selker@oregonstate.edu

Introduction to the report

Over the past year the project had extensive activities in two important Oregon Watersheds. Given the proximity of the project to completion, several of these efforts have lead to rather extensive write-ups, which will soon be submitted for publication. These are included here as appendices.

In the Walla Walla river basin we continue to probe the ability to characterize stream thermal regimes using Distributed Temperature Sensing (DTS). Using black and white cables we were able to measure the solar radiation simultaneously at hundreds of locations both in the Walla Walla and John Day basins. These results are described in Appendix 1.

The spatially-explicit measurement of stream loss and gain is a high priority for us so that we might be able to identify locations of groundwater upwelling that would be useful in targeting restoration that captures this cool water. A technique to achieve this is described in Appendix 2, including a field trial of the method in a constructed wetland.

The key application of the DTS methods relevant to this project is in understanding stream dynamics, particularly spatial and temporal temperature patterns, which can be used to assess habitat suitability, estimate hyporheic exchange, and groundwater inflow. The first major trial of this method is presented in Appendix 3, where the first year (2008) field data obtained by DTS in the Middle Fork of the John Day River is explored.

Appendix 1

Determination of Stream Solar Exposure using Black and White Fiber Optic Cables with DTS.

Shade Estimation Over streams using Distributed Temperature Sensing

Petrides[1*], A., J. Gabrielli[1],A. Arik[1], N. Van de Giesen,[2] and J.S. Selker[1]

Running Title: Distributed Stream Shade Monitoring

For Submitted for publication 12-09 to: Environmental Science & Technology

1 Biological & Ecological Engineering, rm 116 Gilmore Hall, Oregon State University, Corvallis Oregon, 97331-3906 USA. 541-737-2082

2 Civil Engineering & Geosciences, Delft University of Technology, PO Box 5048,

2600 GA Delft, Netherlands, Phone: +31 (0)15 2787180

*corresponding author, petridea@onid.orst.edu

Abstract

The characterization of temporal and spatial distribution of sunlight is essential for understanding energy delivery to natural systems, for example modeling temperature dynamics of streams. Fiber Optic Distributed Temperature Sensing (DTS) allows meter-resolution measurements of temperature for multi-kilometer segments at sub-minute resolution. The contrast in temperature of a pair of helically twisted black and white fiber optic cables was measured with a DTS to document areas exposed to sunlight over the Walla Walla River and Middle Fork of the John Day River, and over grass. A high correlation (R^2 =0.99) was found between DTS-based results and manual field observations of effective shade. These results support the contention that this method can be used for estimating the effective shade at fine spatial resolutions.

Introduction

The use of Distribute Temperature Sensing (DTS) with fiber optic cables to measure temperature with high spatial (1m) and thermal (<0.1˚C) resolution over continuous spans (>10 km) has created great potential to study environmental dynamics (Selker et al., 2006a). DTS fiber optics recently have been used to study streams, wetlands, mine shafts, lakes, and snow packs (Selker et al., 2006b, Lowry et al., 2007, Moffett et al., 2008, Tyler et al., 2009,). This paper presents a demonstration of concept of a technique to quantify meter by meter exposure to solar radiation along km-scale transects using differences in temperature observed between white- and black-jacketed fibers optic cables.

Effective shade is the percentage of the total solar radiation available above a canopy that does not reach the surface of interest. Effective shade is of great importance in stream temperature modeling since solar radiation represents the most significant input of energy (Westhoff et al., 2007, Ringold et al 2003). Several methods have been employed to measure effective shade over streams (for a review of these see Boyd 2004). Methods include manual delineation (Solar Pathfinder Inc.,); analog recorders (Campbell-Stokes Pattern Sunshine Recorder, Nova-links Inc); as well as numerical methods to interpret canopy closure using hemispherical canopy photography (WinScanopy, Regent Instruments, Canada).

The aforementioned methods for estimating effective shade lack fine spatial resolution. They also provide static values rather than documenting time-varying conditions. Effective solar radiation is not uniformly distributed under natural systems where most of the provided shade comes from vegetation. Effective shade changes during the day and through the seasons, due to changing cover (e.g. deciduous trees) and solar angles. The Distributed Temperature Sensing (DTS) technology used in these experiments can continuously record data at spatial resolutions as fine as 0.25 m and lengths exceeding 10 km in time intervals of seconds. The goal of this paper is to verify the feasibility of this approach to temporal delineation of solar radiation over river reaches.

Material and Methods

The fiber optic cable assembly consisted of two (one black and one white) 900 µm O.D. sub-cables helically wound with 10 wraps per meter. The helical winding assured symmetric environmental conditions for the two sub-cables. Each sub-cable consisted of a sheathed multi-mode fiber (250µm O.D. elastomeric tight buffered 50/125 µm multimode graded index fiber) with an aramid strength member contained in a polyurethane outer jacket (part number: 56 AFL Telecommunications, Duncan, NC) (Figure S1). The installed cables were supported on 1 m electric fence posts (Supplement Figure S2). In the Corvallis experiment, the cable was laid out in a serpentine geometry (Supplement Figure S3) over a grass location (9m by 7m), the north side of the installation had more exposure to solar radiation than the south side for the entire duration of the experiment and the west side had more exposure than the east side in the afternoon. During the experiments on the Walla Walla and John Day Rivers, the cables were severed by wildlife. The fiber length unaffected by this damage is listed in Table 1. The original installation for the cable length in both experiments was 1.2 km.

The temperature of the black cable and the white cable depends on solar radiation, wind speed, and air temperature. The **difference** in temperature between the black and white cables deployed side-by side is expected to depend primarily on the solar radiation, being essentially independent of air temperature, but with a second-order dependence on wind speed. In this paper we focus on the first order effect to demonstrate feasibility. Analysis of wind effects will be addressed in following research. The underlying idea is that air temperature and wind will affect both cables equally, as the cables tend to have a temperature difference of less than one degree centigrade. Solar radiation will warm up the black cable significantly more than the white cable due to difference in short-wave albedo. In principle, this should allow high resolution observation of effective shade where the cumulative difference of temperature over time between a location receiving 100% of solar radiation and a location where sunlight is blocked is considered the effective shade.

Temperatures measurements were collected by utilizing a DTS system recording at 5 min and 0.5 m resolution. The system was run for 24 hrs at three locations: 1) The Walla Walla River (45˚59’N 118˚22’E), a third order stream on the north east side of the state of Oregon, USA; 2) Corvallis, Oregon(44˚34N’ 123˚17W), at a grassy location on the Oregon State University (OSU) campus; and. 3) Middle Fork of the John Day River(44˚38’N 118˚39’W), a second order stream on the northeast side of the state of Oregon, USA (Table 1). Solar radiation and air temperature were obtained from proximal weather stations of the Pacific Northwest Cooperative Agricultural Weather Network (AgriMet).

Calibration and Validation

Generally, DTS measurements require in situ calibration of offset, gain, and slope parameters. In this experiment we were particularly concerned with the accuracy of the differences in temperatures between the white and black cables rather than absolute temperatures, thus precise offset values were not required. The global offset was computed based on measurements of night-time air temperature from nearby weather stations for the John Day and Walla Walla tests, while in the Corvallis experiment, a more rigorous calibration provided all three parameters based on measurements from a pair of five meter coils of fiber resting in ice and warm (30˚C) water baths.

For the purposes of this analysis an area was considered to receive solar radiation when temperature differences between the black and white cables on 2 m, 30 min resolution were statistically significant (p-value<0.05), and when at the same time solar radiation measured at a weather station was > 100 W/m^2 (Table 1). Validation here refers to the degree to which alternative measurements of shade distribution correspond to the results obtained by the fiber optic method. In the Walla Walla River a Solar Pathfinder™ was used to compare results of the estimated effective shade by linear regression of both methods.

The cumulative difference (ΔC) in temperature between black and white cables was calculated as:

$$\Delta C = \sum_{1}^{n} (T_B - T_A) \qquad (1)$$

Where: ΔC = Cumulative difference [C˚]

T_B = Temperature of the black cable at x location [C˚]

T_A = Temperature of the white cable at x location [C˚]

n= Number of periods (here taken in 30 min increments) with significant solar radiation

Results and Discussion

This section will begin by observing the development of the cumulative difference of temperature, which is then compared to an independent measurement of effective shade. The entire temperature distribution of the cables in time and space for the two river experiments is presented.

To reduce noise, the 0.5m, 5 min (figure1) data were averaged over 2 meters (4 length points) and over 30 minutes (6 measurements) to compute ΔC (figures 2 and 3). In the John Day River experiment, three peaks of solar radiation were reported from the Agrimet weather station at 11:00, 12:45, and 15:30 hrs (figure1), which were reflected in the DTS data (figure 2). The variability of solar exposure along the river is especially evident during the brief event at 15:30.

During the Walla Walla experiment, manual observations of shade distribution were made at four locations (figure 3b). These observations showed remarkable linear correlation with the cumulative difference of temperature between fibers (regression coefficient R^2 of 0.998, figure 4). Using this relationship, the effective shade was estimated for each 2 m segment of the fiber optic deployment, showing considerable structure in the shade in this vegetated riparian system (figures 5).

For the John Day River experiment manual observations were not available, so the distribution of shade was estimated based on the results of the Walla Walla River. The relationship between cumulative difference and effective shade was assumed to be linear, with the highest cumulative difference corresponding to an unshaded location, and the lowest cumulative difference taken to represent 100% shade (Figure 6). The location of expected full exposure and full shade were verified from field notes in the Walla Walla River.

Conclusions

Field experiments at three sites demonstrated that a DTS fiber optic system is able to provide high temporal and spatial resolution delineation of solar exposure. This was achieved by using a duplex cable made up of black and white sub-cables. The cumulative temperature differences between the black and white cables was found to be linearly related to the measured percentage of shade, providing a relationship for interpretation of the spatially and temporally distributed data.

Significant limitations of the method include:

- Requirement of independent field observations to quantify the fraction of shade.
- Exposure of the cable to damage in a natural environment (animals, falling limbs, etc.).
- Second-order effects of wind on ΔC.

Measuring the effective shade distribution using fiber optic cables has the advantage of providing meter and minute resolution measurements of shade distribution over spans exceeding 5 km. The data provided at such fine resolution is useful for stream temperature modeling, and other biological assessments.

This work describes a proof of concept of this method. Many aspects will benefit from additional study, including: additional analysis of heat exchange effects of wind; the relationship between cable diameter and response; the effect of having the black and white cables touching versus with an air-gap separation; the influence of cable composition and pigment; the effects of solar aging and the accumulation of contamination on the cables; and methods to enhance durability and reduced need for maintenance. For the foreseeable future we believe that the method will require co-located wind, temperature, and solar radiation measurement at a minimum of one full-sun location, and ideally at an additional full-shade location. The method is not inexpensive, with the DTS unit costing >$20,000 and the cable about $2/m. Installation and operation are labor intensive at about one person day per 500 m. Also a continuous power supply is required. Finally, data analysis is involved and time consuming. With further development some of these limitations will diminish, but clearly this method should be undertaken only in cases where simpler approaches are insufficient to address the data needs of the project.

Acknowledgments This research was in part supported by the Walla Walla Watershed Council, the Oregon Watershed Enhancement Board, and the National Science Foundation (NSF EAR- 0711594). Field work at Walla Walla site was provided by Bob Bower, Troy Baker and Nella Parks. The John Day Experiment was supported by the confederated tribes of Warm Springs with field work by Kace Fujiwara. The Corvallis experiment profited from the collaboration in the field by Mary Bowen.

References

Boyd, M., Kasper, B. (2004), Analytical Methods for Dynamic Open Channel Heat and Mass Transfer, Methodology for the Heat Source Model Version 7.0. Available at http://www.heatsource.info

Moffett, K.B., Tyler, S.W., Torgersen, T., Menon, M., Selker, J.S., Gorelick, S.M. (2008), Processes Controlling the Thermal Regime of Saltmarsh Channel Beds, Environmental Science and Technology. 42 pp 671-676

Lowry, C.S., Walker, J., Hunt, R., Anderson, M., (2007), Identifying spatial variability of groundwater discharge in a wetland stream using distributed temperature sensor, Water Resources Res. 43:W10408.

Pacific Northwest Cooperative Agricultural Weather Network, AgriMet. (2009), U.S. Department of Interior operated and maintained by the Bureau of Reclamation. Available from: http://www.usbr.gov/pn/agrimet/

Ringold, A.L.., Van Sickle, J., Rasar, K., Schacher, J., (2003), Use of hemispheric imagery for estimating stream solar exposure, Journal of the American Water Resources Association. No. 02088 pp1373- 1384

Selker, J., Van De Giesen, N., Wethoff, M., Luxemburg, W., and Parlange, M.B. (2006a), Fiber optics opens window on stream dynamics, Geophysical Research Letters 33: L24401

Selker, J.S., Thevenaz, L., Huwald, H., Mallet, A., Luxemburg, W., Van de Giesen, N., Stejskal, M., Zeman, J., Westhoff, M., and Parlange M.B. (2006b), Distributed fiber-optic temperature sensing for hydrologic systems, Water Resources Research. 42:W12202

Tyler, S.W., J.S. Selker, M.B. Hausner, C.E. Hatch, T. Torgersen, C.E. Thodal, and S.G. Schladow (2009), Environmental temperature sensing using Raman spectra DTS fiber-optic methods, Water Resources Research, 45, W00D23

Westhoff, M.C., Savenije H.H.G., W.M.J. Luxemburg, G.S. Stelling, N.C. van de Giesen, J.S. Selker, L. Pfister, and S. Uhlenbrook (2007), A distributed stream temperature model using high resolution temperature observations, Hydrological and Earth Systems Sciences, 11, 1469-1480

Figures

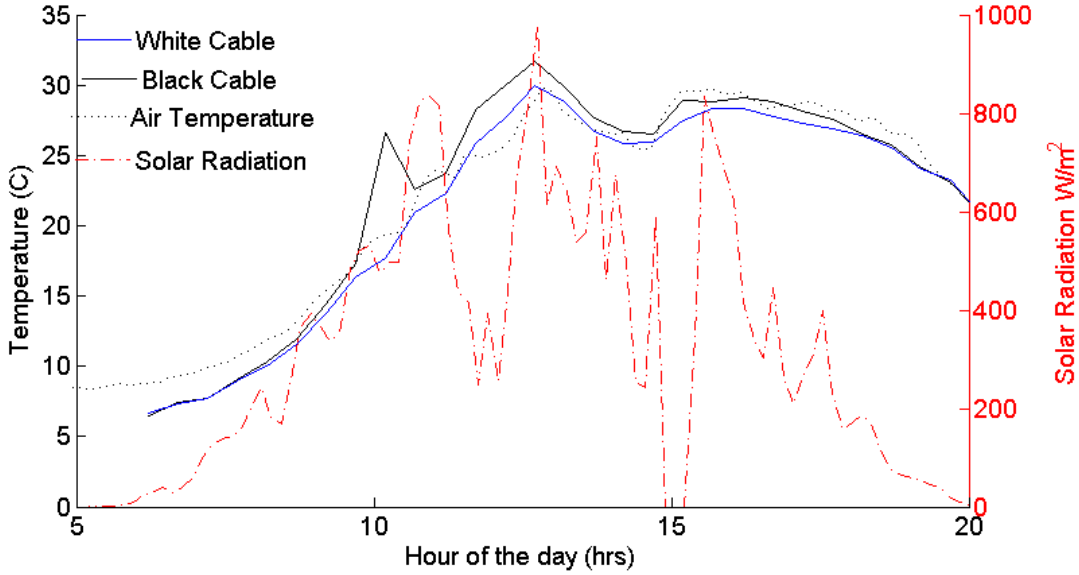

Figure 1. Time series of reported temperature of the white and black fiber optic cables at a single point (150m from the source) in the John Day experiment. Air temperature and solar radiation were used as reference for the entire river segment.

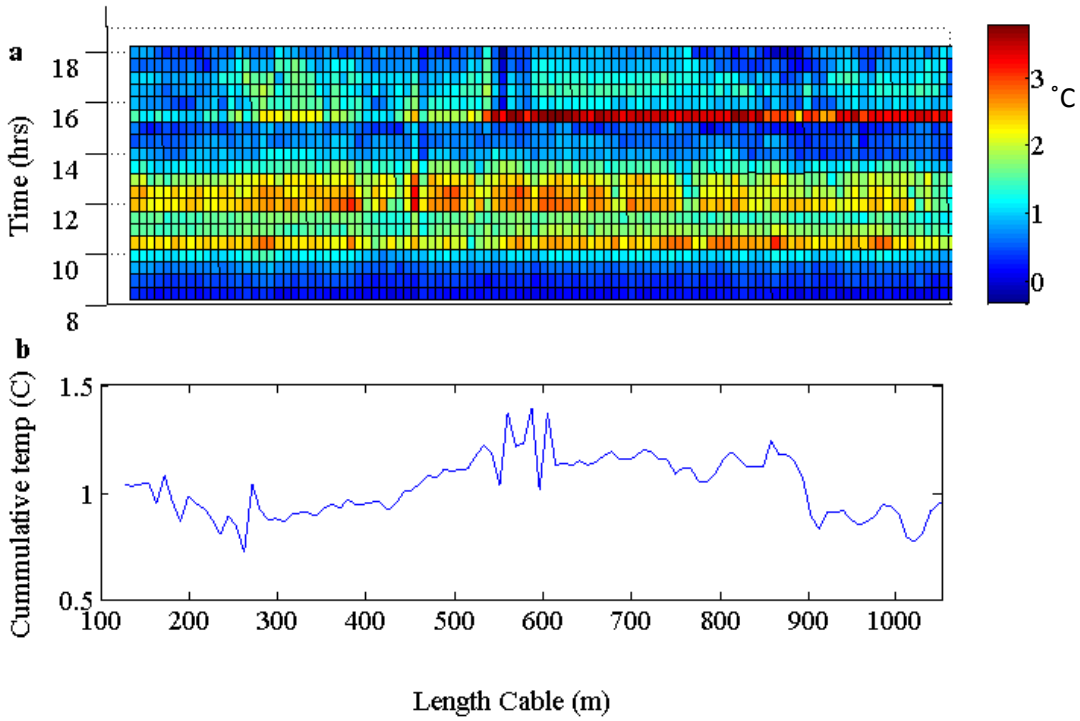

Figure 2. John Day experiment, (a) Distribution of difference in temperature over 2 meters in space (horizontally) and 33 minutes in time (vertically). (b) Difference of temperature for the day of measurement.

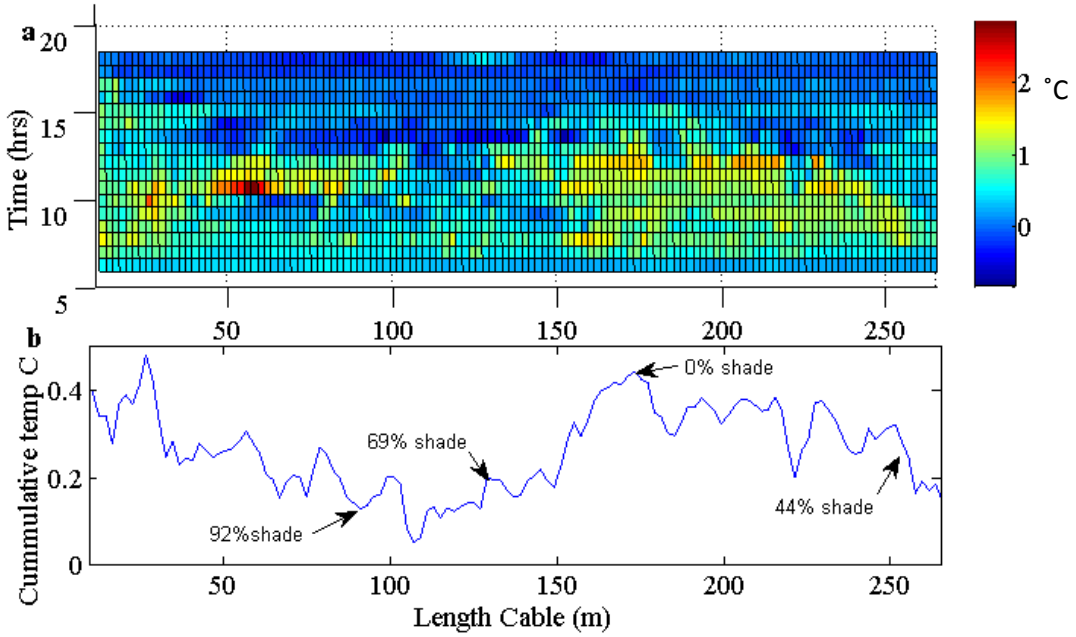

Figure 3 (a) Walla Walla distribution of difference in temperature, average in time over 30 minutes (vertically) and averaged over 2 meters in space (horizontally). (b) Difference in temperature along the cable. Marked shade percentages are observations taken with Solar Pathfinder.

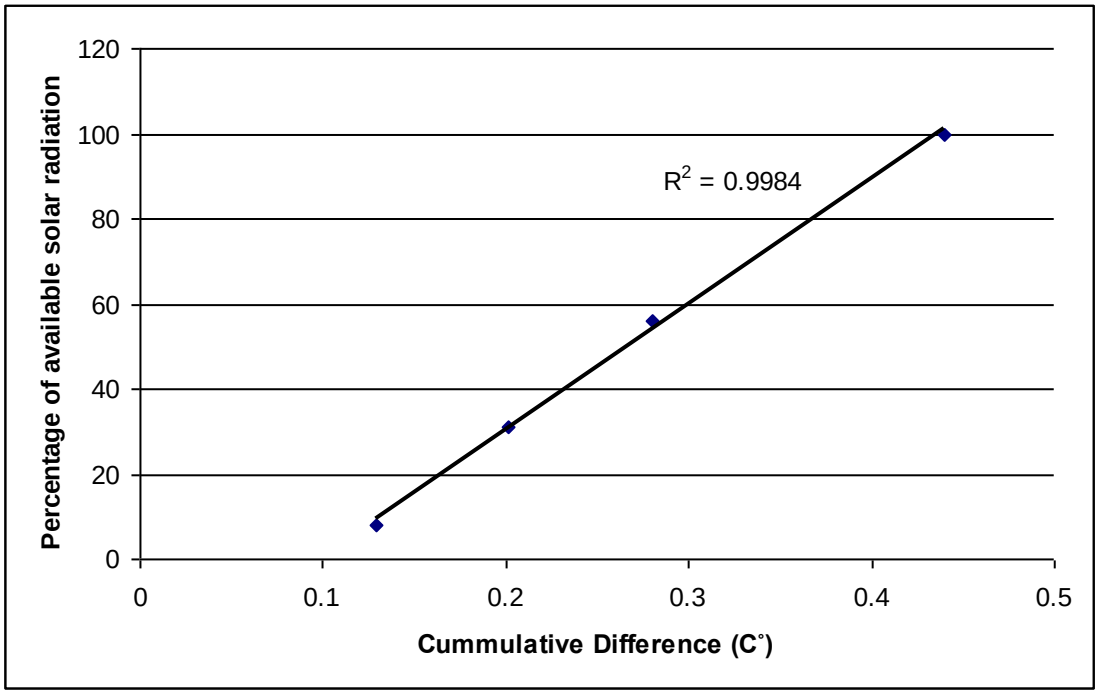

Figure 4 Comparison between Solar pathfinder measurements and cumulative difference in the fiber optic cables. The linear least-squared fit between the data is shown as a line, with an R^2 of 0.998.

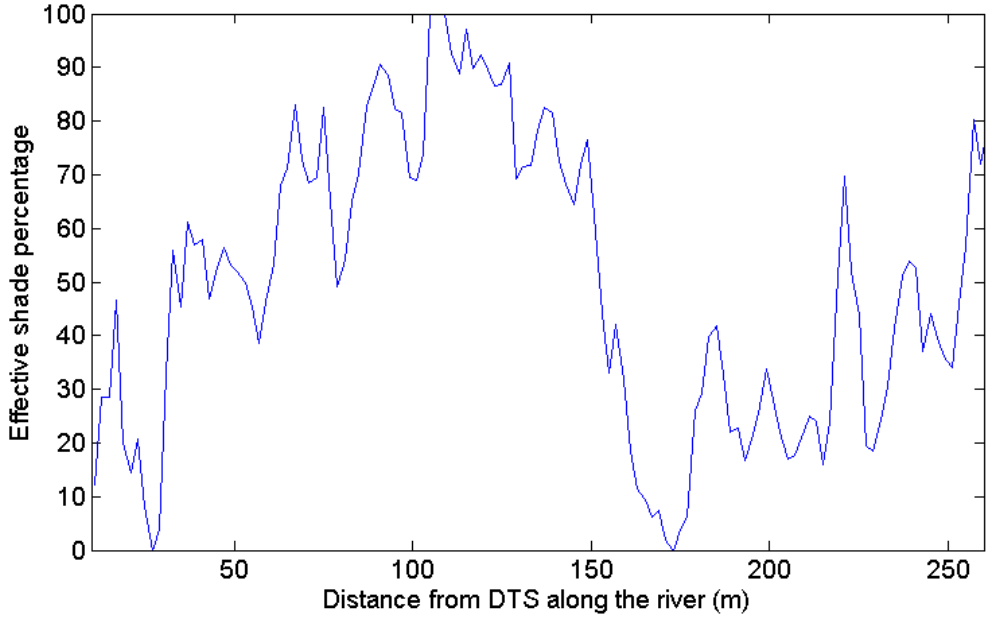

Figure 5 Effective shade distribution in the Walla Walla River as a percentage for the daytime hours of 09/16/2008.

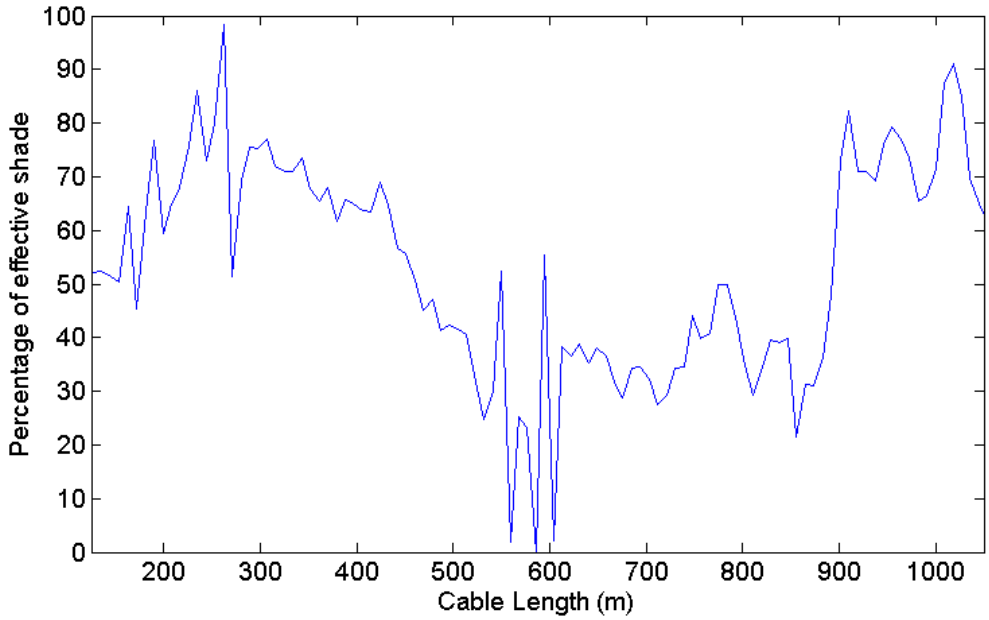

Figure 6 Effective shade distribution in the John Day River as a percentage for the daytime hours of 08/06/2008.

Tables

Table 1 Technical feature of the three cable deployments.

Location	Date	Cable length (m)	Period of the day with significant solar radiation (hrs)	Min. solar radiation (W/m^2)	Peak solar radiation (W/m^2)	Average temperature. Diff. between cables. (˚C)
Walla Walla 45˚59'N 118˚22'E	09/16/2008	265	8:00 to 16:00	194	704	0.73
Corvallis 44˚34N' 123˚17W	10/19/2008	400	9:00 to 17:00	100	600	2.53
John Day 44˚38'N 118˚39'W	08/06/2008	1000	8:00 to 18:00	182	800	1.89

Supplemental Materials

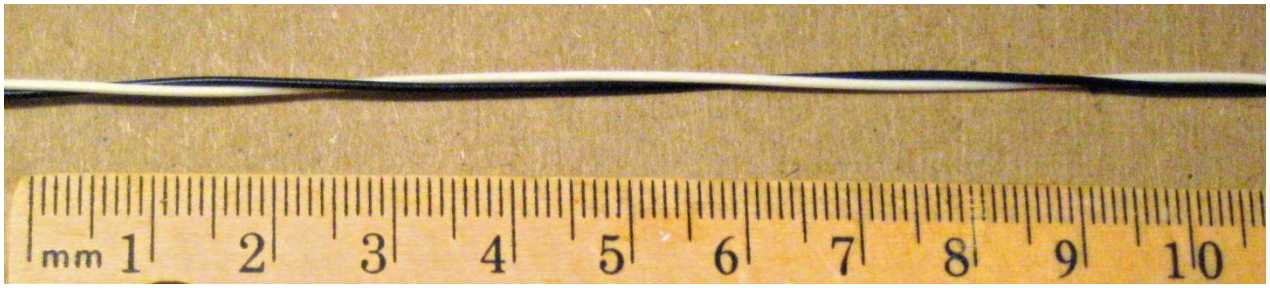

S1. Photograph of fiber optic cable used in the experiments. The individual black and white cable elements are 900 µm O.D., and they are twisted to provide, on average, one full helical rotation per 0.1 m

S2. Photograph of Arístides Petrides deploying the cable in the Walla Walla River, having just passed the cable through a support post.

S3 Photograph of Corvallis experiment deployment. Note shade from tree crossing the right-hand fibers.

Appendix 2: **INFILTRATION CHARACTERIZATION USING DTS: CASE STUDY OF A CONSTRUCTED WETLAND**

INFILTRATION CHARACTERIZATION USING DTS: CASE STUDY OF A CONSTRUCTED WETLAND

Chris Gregory, John S. Selker, Ryan Stewart, Daniel Moreno

Department of Biological and Ecological Engineering

Oregon State University, Corvallis, OR 97331

For Submission to *Hydrology and Earth System Sciences*

1 Abstract

This study characterizes the infiltration of an unlined surface flow wetland observed in the summer and early fall of 2009. The wetland was approximately 0.15 ha and was constructed in a river floodplain using native silty clay loam from the Wapato series classification. The purpose of the wetland was to demonstrate the feasibility of using treatment wetlands for temperature and ammonia reduction in wastewater effluent. Infiltration was determined as the daily residual of a wetland water budget. Infiltrative variability was characterized with a distributed temperature sensor (DTS) by applying heat pulses to a subsurface fiber optic cable. Infiltration losses exceeded outflow losses for most of the study, but steadily decreased over time. Infiltrative variability was within a factor of 2 and also decreased over time. Soil clogging processes, settling, and instrument error are offered as reasonable explanations.

2 Introduction

The City of Woodburn's Wastewater Treatment Plant (WWTP) is currently investigating natural alternative systems for improving the quality of its effluent. Based on the current limits for allowable discharge into the Pudding River outlined in the WWTP's NPDES permit, temperature and ammonia restrictions will be annually exceeded by 2020 in the summer and early fall (Healy and Madison, 2006).

In order to avoid future NPDES violations, the City of Woodburn has constructed several pilot-scaled natural systems to assess their potential for improving wastewater quality and inform decisions regarding future WWTP operations. One of the pilot systems, a 0.15 ha free surface flow wetland, was developed in the floodplain of the Pudding River near the WWTP site. The wetland was designed to reduce effluent temperature and ammonia levels before reaching the nearby Pudding River. Monitoring of wetland temperature treatment was conducted in 2009 and has been presented in chapter 2.

Further, monitoring wetland infiltration was also necessary to understand the pilot system performance. The surface flow wetland was constructed with native floodplain soil material and expected to exhibit substantial leakage into the underlying silty sand aquifer. Pre-existing drainage tiles throughout the floodplain in unknown locations were suspected to make preferential drainage pathways an additional concern. Consequently, for designers and city officials considering the impact of larger wetlands at the WWTP site, assessment of total infiltration and infiltration variability in the pilot wetland was critical to understanding the local area's hydraulic potential.

The objective of this study was to characterize infiltration in the pilot wetland during operations in the summer and early fall of 2009. System-wide infiltration was calculated using a wetland water budget, and additional information about infiltration variability was obtained using a heat pulse method on a distributed fiber optic cable located approximately 25 cm below ground. Temperature from the fiber was collected with distributed temperature sensor (DTS) systems. Based on the findings of this research, conclusions about the infiltration characteristics observed were passed on to those responsible for potential wetlands expansion at the WWTP.

2.1 The Wetland Water Budget and Infiltration

Understanding the flow through a treatment wetland can begin with a simplified determination of water inputs and outputs. While assessing the actual rates of these processes can be difficult and commonly imprecise, they nonetheless comprise the broader

framework for understanding the hydrology of the system. Figure 1 shows the inputs and outputs flows involved in the wetland water budget.

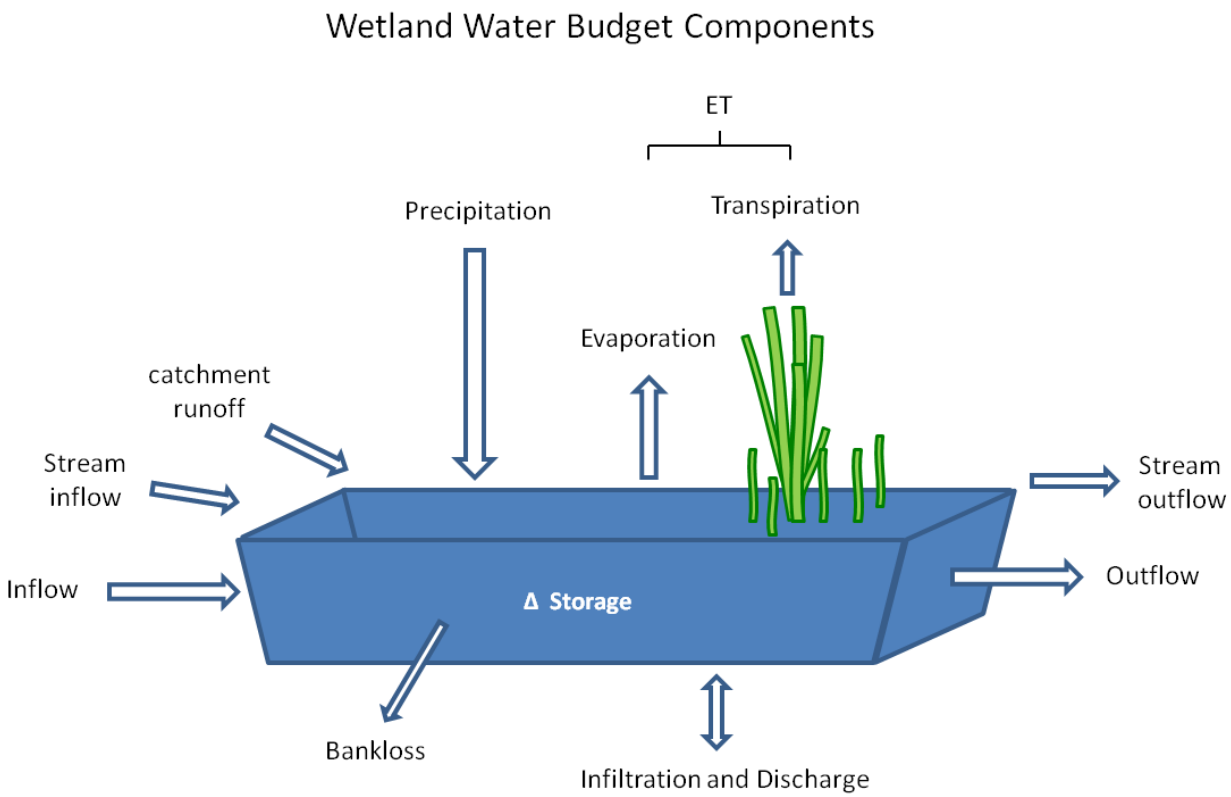

Figure 1 Components of the wetland water budget. (adapted after Kadlec and Wallace, 2008)

The main processes contributing water to the wetland, referred to as inputs, include the volumetric inflow coming from the WWTP, potential stream contributions or catchment runoff, local groundwater discharges into the wetland, and precipitation. In the present study of the Woodburn pilot wetland, constructed berms around the perimeter of the wetland cell prohibited catchment runoff, and the nearby Pudding River was blocked from entering the floodplain by a temporary culvert plug during the operation period in the summer. In addition, the local groundwater table under the wetland sat well below the ground surface and did not contribute to surface water flow. The input components were then reduced to precipitation, which was extremely little in the summer and early fall, and volumetric inflow.

The processes contributing to the water outputs include volumetric surface outflow, groundwater recharge, or infiltration, lateral bankloss through perimeter berms, and evapotranspiration. Depending on the type of wetland, its vegetation, climate, geology and construction, the relative magnitude of each output can vary greatly. For example, in a surface flow wetland that has been lined with 30 cm of compacted clay to prevent mixing with underlying groundwater, infiltration may be insignificant and surface outflow may account for most of the exiting water. However, in the case of an unlined surface flow wetland, such as at the Woodburn WWTP, infiltration may be comparable or at times even exceed outflow.

Lateral bank losses can be a significant infiltration component where the perimeter-to-area ratio of the wetland is relatively large. In this case, hydraulic gradients through the confining banks may be much greater than vertical infiltration through the bottom of the wetland basin, contributing to higher rates of lateral infiltration at these locations. Lateral bankloss becomes less significant when the water level in the wetland is lowered and the hydraulic gradients through the banks are reduced. Evapotranspiration depends on the climate, season and vegetation in the wetland. Often, evapotranspiration can be estimated by using atmospheric data from national weather stations and applying a crop-based conversion coefficient.

To close the water budget, the volumetric change in wetland water storage is needed. This term can be related to the water depth if the internal wetland geometry is uniform or a detailed survey of the internal bathymetry has been conducted. In many natural wetlands, the bathymetry of the wetland is quite complex, owing to irregular landscape features as well as changing depositional processes and thicknesses of accumulating sediment. This makes relating the water depth at a monitored location to volume of water in the entire wetland system quite challenging. However, many constructed wetlands operate with rather simple geometries that allow accurate estimation of the total volume stored.

In wetlands that are used as advanced treatment to polish the water quality and where there is no perceived threat to groundwater contamination, infiltration may be allowed without the use of a restrictive lining. Leaky wetland systems may also be opted for when the infiltrating water is expected to be diluted through discharge into a nearby river (Kadlec and Wallace, 2008).

The processes that govern groundwater infiltration are complex, as issues arise out of the unique placement, hydrogeology, water quality, vegetation and operation of any particular

wetland. In a wetland with significant leaking and a relatively shallow water table, infiltration below the wetland may saturate the underlying porous media and begin to mound on the piezometric surface. If mounding is large enough, the hydraulic gradient of infiltration will be reduced, leading to lower infiltration rates over time. However, confining layers in the underlying subsurface may complicate this process leading to mounding at shallower depths and/or lateral flow away from the local piezometric surface.

Infiltration through treatment wetlands has also been shown to vary significantly based on the quality, loading rate and duration of applied influent (Kadlec, 2008). In low quality wastewater with high total suspended solids (TSS), biological oxygen demand (BOD), nitrogen and ammonia levels, clogging in the top horizon of wetland soil is well established (Van Cuyk, 2001; Blazejewski, 1997; Kadlec and Wallace, 2008). Formation of a clogging layer is especially acute in horizontal subsurface flow wetlands and vertical infiltration wetlands (Knowles, 2009; Langergraber, 2003), however the same processes may occur in leaky surface flow wetlands that operate similarly to recharge basins (see Bouwer and Rice, 1989, on clogging processes in recharge basins).

The clogging of wetland soil surfaces has been attributed to a number of contributing processes. According to the literature, the main causes are the grain distribution and pore sizes of the bed material, deposition of suspended solids in the soil pores, accumulation of organic material resistant to microbial degradation in the soil biomat formation of microbial biofilms on the soil surfaces, development of plant roots and rhizomes that occupy pore volume, and chemical precipitation and deposition in the pore spaces (Blazejewski, 1997; Kadlec and Wallace, 2008). These processes effectively reduce the hydraulic conductivity of the wetland by decreasing the porosity of the top layer of soil. In this situation, the infiltration rate in the wetland becomes limited by the hydraulic conductivity of the clogging layer. Further, hydraulic conductivity has been shown to be extremely sensitive to porosity, decreasing by about a factor of 10 when porosity is reduced by one-third (Kadlec and Wallace, 2008).

Taken together it is apparent that prediction of the spatial distribution of percolation under a wetland is bound to be imprecise. We therefore decided to directly measure spatial distribution of percolation using fiber optic temperature sensing.

2.2 DTS and the Heat Pulse Method

Distributing Temperature Sensing (DTS) background, theory, and system components have already been discussed in some detail in chapter 2. A brief review is provided here.

DTS systems were first developed two decades ago and use optical fibers as temperature sensors (Dakin et al., 1985; Kurashima et al., 1990). High frequency light transmissions are emitted by DTS systems through the optical fibers while an optical sensor records the frequencies and amplitudes of backscattered photons. The arrival time of returning backscatter is recorded by the DTS, while Brillouin and Raman scattering principles are applied to the backscattered photons to calculate fiber temperatures. Based on the arrival time data and the speed of light in the optical fiber, the calculated temperatures are associated with positions on the optical fiber. The result is a detailed temperature profile across the length of the fiber with accuracies approaching 0.01°C and spatial resolution up to 0.25 m (Selker et al., 2006).

Methods for extracting soil properties and water content through heated probes have been well established (Byrne et al., 1968; Mori et al., 2003; Tarara et al., 1997). These methods are based on quantified heat inputs being applied to porous media and the resulting thermal response being monitored by temperature sensors. In single-probe configurations, the heating component and temperature sensor are co-located on the same probe device. In multi-probe configurations, one probe typically serves as the heated element while the other probes monitor the thermal response of the media at fixed distances from the heated element (Basinger et al., 2003; Bristow et al., 1994). As heating methods have become more useful for determining soil properties and water content, numerous techniques for quantifying water flux with heated probes have also been investigated (Hopmans et al., 2002; Wang et al., 2002; Mori et al., 2005).

More recently, several studies have incorporated fiber optic cables into single-probe heat pulse methods. These studies have utilized the protective metallic jackets found on many fiber optic cables as electrical resistors, capable of heating the cable uniformly across its length. DTS systems were then used to extract temperature profiles from the cable to monitor its thermal response to the heating based on its location of deployment. Weiss (2003) and Perzlmaier et al. (2004) both investigated thermal conductivities and water contents of soils using heated fiber optic cables. Their methods involved cable heating for an extended period of time, followed by calibration equations fitted to the slope and intercept of resulting thermal responses. Sayde et al. (2009) followed this work with an alternative approach for calculating soil moisture content. His method used the integration of the total change in fiber temperature to distinguish between soil moisture contents.

Several studies have also demonstrated the capability of DTS fiber optic applications to measure water flux in porous media. Johansson et al. (2004) and Velasquez et al. (2007) used fiber optics in the monitoring of localized seepage in embankment dams and earthen structures. Their techniques were passive measurements that relied on temperature gradients to reveal seepage, and where feasible, quantify flux. Perzlmaier et al. (2004, 2006) investigated the use of actively heated fiber optics for determination of seepage velocity.

They applied numerical methods to laboratory and field data for total rise in temperature, and found that analytical and DTS results were quite agreeable (see Perzlmaier et al., 2004). The approach used in this study for investigating relative seepage variability largely followed the methods developed by Perzlmaier et al. (2004, 2006) in respect to monitoring dam leakage.

3 Materials and Methods

3.1 Site Description

A more complete overview of the location, climatic conditions, operational components and vegetation of the pilot wetland can be found in the Materials and Methods section of chapter 2. In general, the wetland was located in the floodplain of the Pudding River near Woodburn, Oregon, within larger context of the Willamette Valley (see Figure 2.2 for a map view of the site). The wetland soil material was classified as silty clay loam in the Wapato series, which locally overlaid a shallow groundwater aquifer that discharged into the Pudding River. Woodburn's WWTP delivered water to the wetland from an uphill storage lagoon, and the hydraulic operation was designed to maintain a 2-day hydraulic retention time (HRT), which translated to a water depth of about 40 cm.

In addition, numerous pre-existing agricultural drain tiles intended to quickly drain the floodplain underlie the surrounding land, providing significant opportunity for preferential drainage pathways. Little certainty exists about the locations and orientations of these drain tiles (which were buried approximately 2 m underground), however several drain tiles directly beneath the wetland were unearthed and plugged in the summer of 2008. The success of this effort to seal the wetland from excessive tile drainage was investigated in this study

3.2 Instrumentation

Two Onset HOBO® U-20 submersible water level loggers, housed in three-foot, drive-tip piezometers, were placed in the north and south ends of the wetland. The piezometers were manually driven halfway down (1.5 feet) into both the north and south deep zones. The U-20 loggers recorded continuous absolute pressures averaged over 10-minute intervals. Details about the treatment of the data and water level calculations were presented in the Materials and Methods section of chapter 2.

Two additional HOBO® U-20s located in nearby piezometers were utilized to interpret the hydrologic response of the shallow aquifer in surrounding areas. These U-20 loggers were operated continuously and averaged over 15-minute intervals.

Two Signet 2552 Metal Magmeter flow sensors (Schaffhausen, Switzerland) were installed in the inlet and outlet locations of the wetland pipe irrigation system. The first sensor monitored flow entering the wetland through the inlet control pipe. The second sensor recorded the only surface flow leaving the wetland through an outlet pipe. Campbell Scientific CR200-series dataloggers recorded continuous flow from these sensors based on 5-minute flow averages. Further information on the calibration procedure undertaken with these flow sensors can be found in chapter 2.

Two Raman-based DTS systems were used in fiber optic temperature collection—a SensorTran 5100 M4 and a Sensornet Oryx. Data was collected on the SensorTran using 1-minute integration times with 0.5 m spatial resolution. The Sensornet Oryx was used with 1-minute integrations and 1 m spatial resolution.

Calibration of the DTS systems were explored using both internal (involving the DTS operating configuration) and external (involving post-processing data alteration) procedures. For data collection with the SensorTran DTS, ice-slush baths kept around 0° C were placed at the ends of each cable segment, while internal adjustments to the calibration coefficients were made within the DTS operating system to match field observations. Light attenuation at the junction of fiber splices necessitated calibration for each continuous fiber segment between splices. After calibration coefficients were assigned for all segments, the DTS produced fairly accurate results (within about 1° C).

With actual temperatures of the ice-slush baths as well as warm-water baths recorded with a high-precision thermometer during many data collections, an external calibration procedure was developed to rectify the data to within 0.1° C (see Appendix A). This calibration procedure took the “roughly” calibrated data from the internal DTS adjustments, then made offset, attenuation, and gain corrections based on field data (see Appendix Figures A.1 through A.8). However, for applications of the heat pulse method that are concerned with changes in temperature rather than the finite accuracy of absolute temperature, this kind of external calibration was found unnecessary. Thus, data collection in later work with the Sensornet Oryx DTS was taken with minimal internal calibrations and no external calibrations.

3.3 Fiber Optic Installation

Over one kilometer of fiber optic cable was strategically emplaced in the top 30 cm of the wetland soil. The cable emplacement was accomplished using a custom steel plow that was designed specifically for this installation. The plow consisted of a large steel base plate that

rested flush with the ground surface, a smaller steel plate that had been inserted through and welded to the base plate, serving as the plow blade, and a two-tiered metal pipe rack extending vertically above the base plate that was used to hold up to four reels of cable at a time (see Appendix Figure C.2). The plow blade was welded to the base plate at a 30 degree angle from perpendicular so that after passing through the ground, the resulting crack would be aided by gravity in re-sealing. Four grooves were reamed into the plow blade, starting from the top edge where the fiber optic cables would enter, and then continuing down the side of the blade and out the back edge where the cables would exit. Four stainless steel pipes were then inserted into each of the grooves to guide the cables into and out of the plow blade. Plow advancement was accomplished by attaching the front end of the plow to the back end a tractor by a sufficiently thick steel cable, and then driving the tractor forward. The leading edge of the base plate was bent upward 30 degrees from horizontal to reduce friction with ground surface and the likelihood of vegetation snags. In addition, the reel racks were designed to incur minimal friction with the reels, allowing the cable to unwind freely with advancement of the plow.

In regards to the fiber optic layout within the wetland, two large U-shaped loops were plowed in both the east and west sections of the wetland (see Figure 2). Each “U” loop consisted of four cables, each about 130 m in length, simultaneously being plowed into the ground at four different depths—10, 20, 25, and 30 cm. (these depths are relative to the plow blade; vertical depths accounting for 30 degree plow blade angle are closer to 8.7, 17.3, 21.7, and 26 cm.) The installation resulted in the emplacement of eight separate segments of cable, all approximately 130 m in length (see Appendix Figures C.3 and C.4). In order to collect temperature data from all of the segments at once, the optical fibers were joined together through a series of fusion splices that ultimately created a single fiber. Since the cables in the study were “duplex” (that is, they contained two fibers) the DTS collected data from both fibers in each cable. Therefore, the sensor length was effectively doubled by utilizing both fibers in the cables, resulting in duplicate temperature measurements for each geospatial location. In all, 16 splices were made across 1025 m of cable, producing a 2050 m fiber length.

To reference specific cables segments, nomenclature was developed based on north/south and east/west divisions. The first division reference refers to either north or south of the middle deep zone. The second reference is either east or west of the middle berm. The last division reference refers to the east or west sides of the shallow area. For example, “NEW” refers to the cables north of the middle deep zone, east of the middle berm, and on the west side of the shallow area (closest to the middle berm).

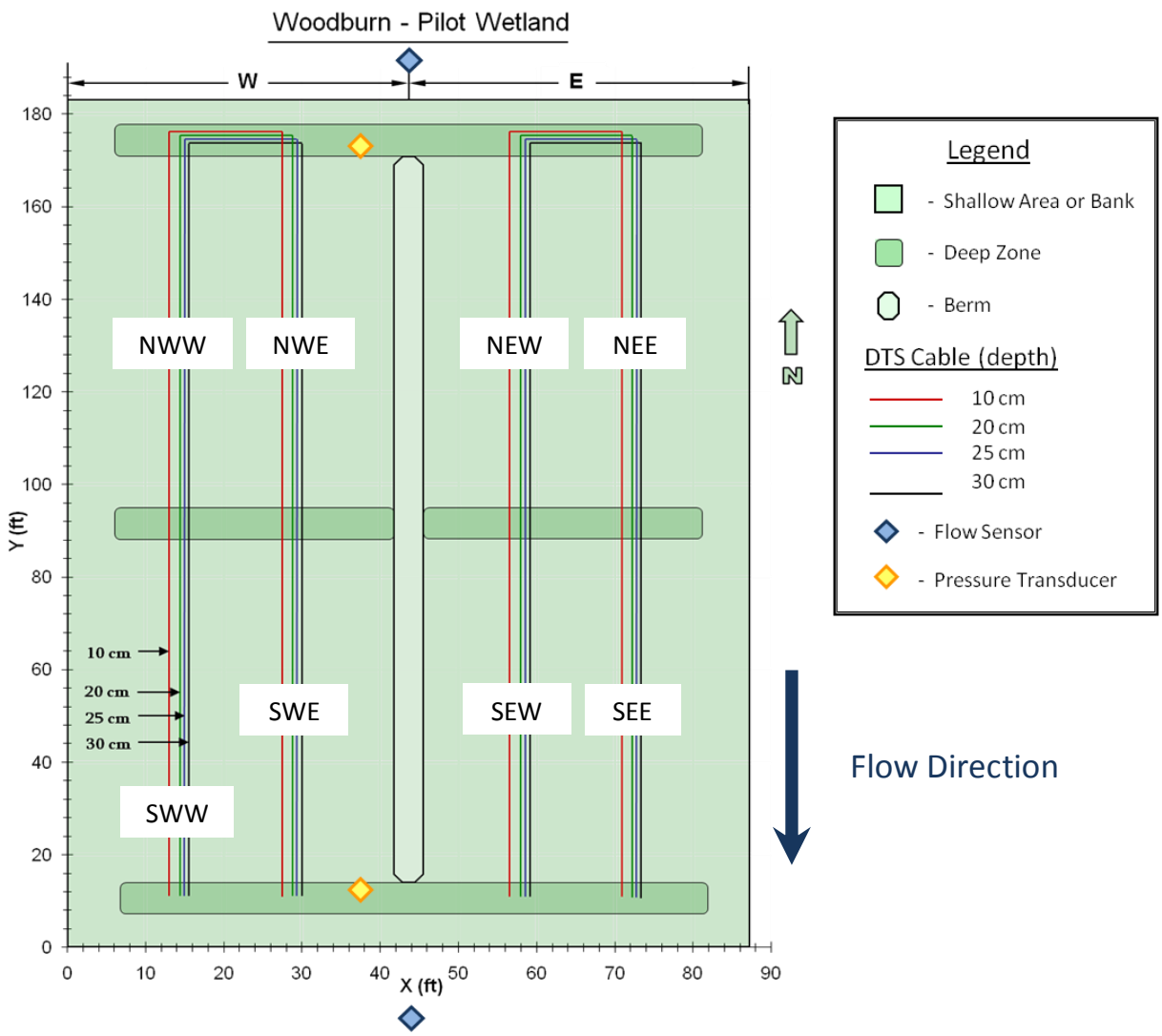

Figure 2 Location of sensors and fiber optic cable depths in pilot wetland. U.S. customary units are used for length dimensions, corresponding to wetland blueprints. Quadrant nomenclature is shown for each of eight subsurface cable segments.

3.4 Components of a Wetland Water Budget

A wetland water budget can be represented by the equation:

$$\text{Flow In} + \text{Precipitation} = \text{Flow Out} + \text{Infiltration} + \text{ET} + \Delta\ \text{Storage} \qquad \text{Eq. 1}$$

The following discusses the data collected and methods used for quantification of each term in the wetland water budget equation.

Flow In

Flow entering the wetland was recorded as 5-minute averages by a Magmeter flow sensor located at the inlet control pipe. This flow value, in gpm, was then converted to a loading rate in cm/day by summing the total volume in, converting from gallons to cubic meters, and then dividing by the area of the wetland. The wetland area was determined using field-validated blueprint dimensions of wetland length and width, accounting only for the internal areas covered in water and one additional foot of horizontal berm area at each boundary (Figure 3).

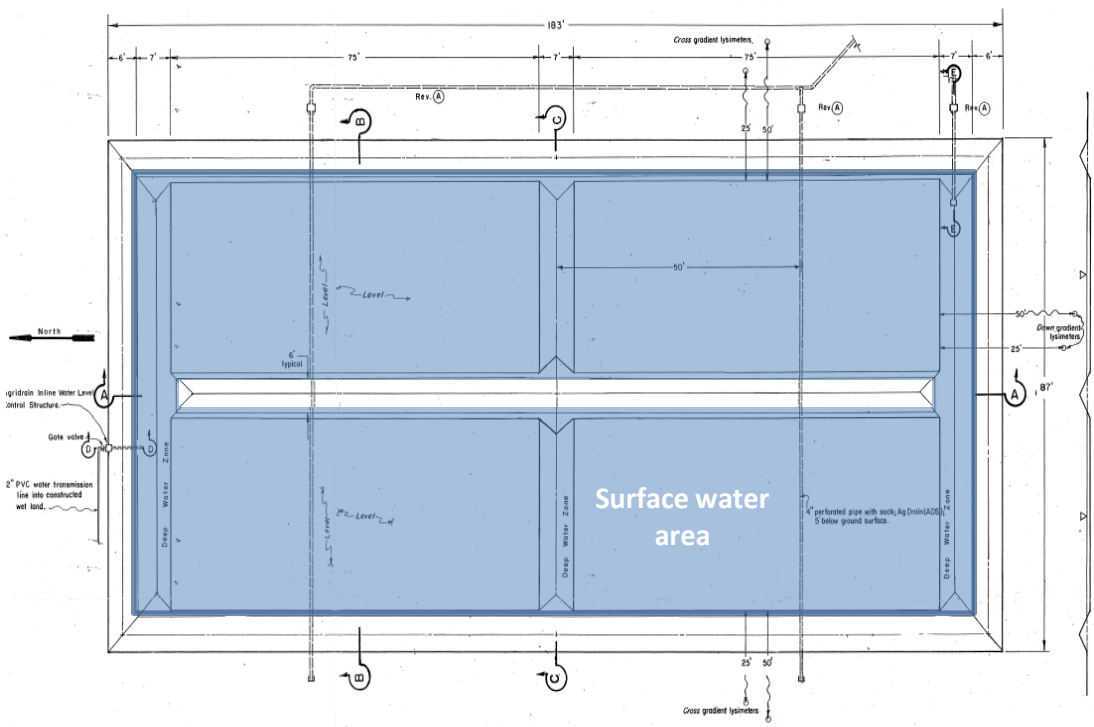

Figure 3 Blueprint of pilot wetland (in US customary units). Surface water area used for loading rate calculations is represented in blue, excluding the middle and perimeter berms.

The length and width dimensions used in the area calculation were:

$$\text{Wetland water area} = (173 \text{ ft} \times 77 \text{ ft}) - (155 \text{ ft} \times 4 \text{ ft}) = 12701 \text{ ft}^2 = 1180 \text{ m}^2$$

where the first term represents the submerged interior area and the second term represents the above-water berm area.

Precipitation

Daily precipitation values were obtained online from the USBR AgriMet weather station in Aurora, Oregon (station ARAO). These values, given in inches, were converted to cm and treated as an additional loading rate term in cm/day.

Flow Out

Flow leaving the wetland was recorded with a Magmeter flow sensor similarly to the flow coming in. The sum of the volume leaving each day was divided by the wetland area to convert to a rate of cm/day.

Evapotranspiration

Daily evapotranspiration (ET) values were calculated using Aurora, Oregon AgriMet weather station data (station ARAO). Output from the Aurora AgriMet station is ET_r, an alfalfa reference, and needs to first be converted to a grass reference, ET_o. Using an AgriMet crop coefficient curve for lawn/turf (essentially reference grass conditions) the following conversion was applied:

$$ET_o = 0.80 \times ET_r \qquad \text{Eq. 2}$$

To calculate crop ET, the following equation was used:

$$ET_c = K_c \times ET_o \qquad \text{Eq. 3}$$

where ET_c refers to the crop ET, and K_c, refers to the crop coefficient. K_c was obtained from FAO document 56 for cattails and bulrushes at most 2 m tall, using the mid-season value of 1.20. The daily value of ET_c was converted from inches and considered as a daily rate of cm/day.

Change in Storage

To account for changes in water storage within the wetland, daily average water levels were determined from hourly pressure transducer data. These averages were then compared across consecutive days to determine changes in water level height and given units of cm/day.

Infiltration

With all other components accounted for, infiltration was calculated as the residual of the water balance equation:

Infiltration = Flow In + Precipitation – Flow Out – ET – Δ Storage

Eq. 4

The continuous data for the above components therefore provides daily infiltration rates through time in cm/day.

3.5 Spatially Distributed Infiltration Rates

In an effort to spatially determine relative variability in infiltration rates, a DTS system was used in conjunction with a subsurface fiber optic cable that was heated for various lengths of time. The cable was a Brusteel (Brugg Cable, Brugg, Switzerland) 4FG5, duplex, multimode cable located at approximately 25 cm depth (see Figure 2). Heating was accomplished by connecting 220 V to the cable's interior steel jacket exposed on the ends of each cable segment. Both heated cable segments (located in the east and west halves of the wetland) had lengths of approximately 105 m. The resistivity of the steel jacket was 440 ohms/km. The total resistance of the cable, R_T, can be calculated as:

$$R_T = R * L = 440\ \Omega\ /\text{km} * 0.105\ \text{km} = 46.2\ \Omega \qquad \text{Eq. 5}$$

and the heat flux per unit length, q_L, can then be determined by:

$$q_L = V^2/(R_t * L) = 220\ V^2/(46.2\ \Omega * 105\ \text{m}) = 9.98 \text{ or } 10\ \text{W/m} \qquad \text{Eq. 6}$$

The following equation, taken from Perzlmaeir et al. (2004) after Wagner (1998), relates change in temperature to the heat flux applied to a coated cylinder:

$$\Delta T = \frac{q_L}{2 \cdot \pi} \cdot \left[\frac{1}{\lambda_m} \cdot \ln\left(\frac{r_a}{r_i}\right) + \frac{1}{\alpha \cdot r_a} \right] \qquad \text{Eq. 7}$$

where ΔT = total change in temperature from heat pulse (K)

q_L = heat flux per unit length (W/m)

λ_m = thermal conductivity of coating ($Wm^{-1}K^{-1}$)

r_a = outer radius of coating (m)

r_i = inner radius of coating (m)

α = heat transfer coefficient

From the data obtained by the DTS system for a one-hour heated period, *ΔT* was determined as the total rise in temperature observed at each meter along the cable. The starting temperature was calculated at each point as the average of three 1-minute integrations taken immediately prior to heating. Figure 4 shows how *ΔT* was determined at each cable location, and Figure 5 shows variability in *ΔT* across a cable segment. Appendix Figures B.1 through B.6 illustrate several examples of variable heating in subsurface cable segments using surfaced plots of hour-long heat pulses.

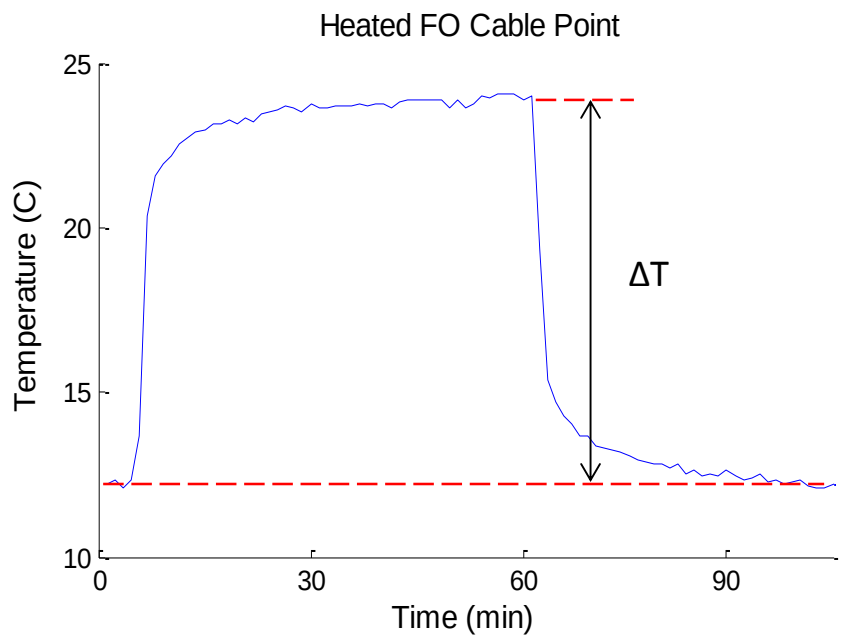

Figure 4 Rise in cable temperature, *ΔT*, observed over heating duration.

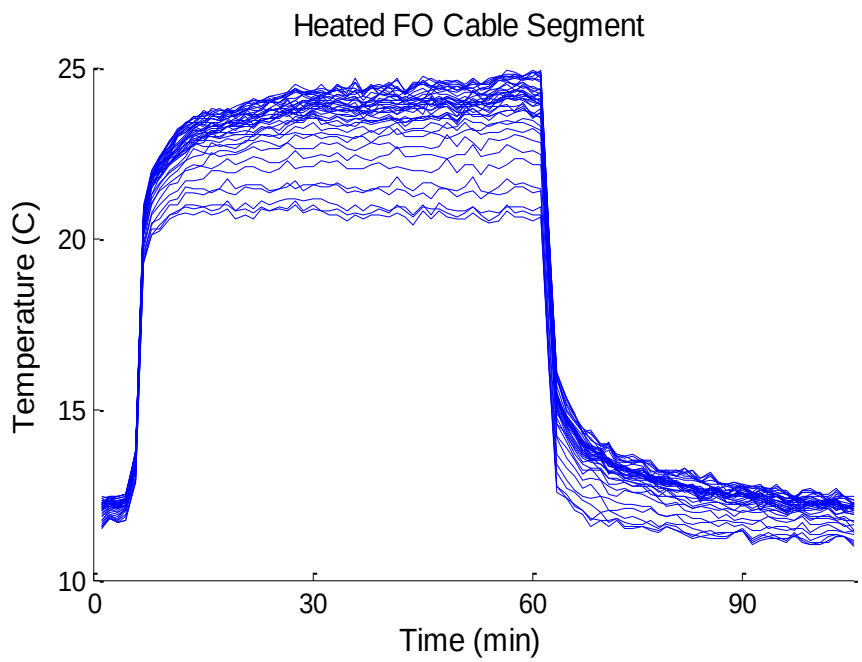

Figure 5 Variation in cable heating response across a 20 m segment.

The manufacturer's specifications for Brusteel 4FG5 were used for the thermal conductivity, the outer radius and the inner radius of the coating. Accordingly, λ_m = 0.25 $Wm^{-1}K^{-1}$, r_a = $1.9*10^{-3}$ (m) and r_i = $1.7*10^{-3}$ (m).

The dimensionless Nusselt number, Nu_D, given for cylinders can be used to express the heat-transfer coefficient, α, as:

$$Nu_D = \alpha \cdot D/\lambda_{fl} \qquad \text{Eq. 8}$$

where D = diameter of the cylinder (m)

λ_{fl} = thermal conductivity of the fluid ($Wm^{-1}K^{-1}$)

The outer diameter of the cylinder used was 3.8 10^{-3} m (manufacturer specifications). Solving the above equations for the heat transfer coefficient, α, gives:

$$\alpha = \frac{1}{\left[\frac{\Delta T \cdot 2\pi}{q_L} - \frac{1}{\lambda_m} \cdot \ln\left(\frac{r_a}{r_i}\right)\right]} = \frac{Nu_D \cdot \lambda_{fl}}{D}$$ Eq. 9

Additionally, the effective Nusselt number for forced convection in a Darcy-flow regime, taken from Perzlmaier et al. (2004) in following with Fand et al. (1993), can be written as:

$$Nu_{eff} = 1.248 \cdot {Re_D}^{0.5} \cdot {Pr_{eff}}^{0.3534} \cdot 1.325 \cdot (\arctan[(D/d)^{0.5}])$$

Eq. 10

where Re_D = dimensionless Reynolds number of a cylinder

Pr_{eff} = dimensionless Prandtl number

d = diameter of the particles (m)

The mean particle diameter used for silty clay loam (the Wapato series classification) was 25 µm (following Muñoz-Carpena and Parsons 2000). Solving for the Reynolds number gives:

$$Re_D = \left[\frac{Nu_{eff}}{1.248 \cdot {Pr_{eff}}^{0.3534} \cdot 1.325 \cdot \arctan[(D/d)^{0.5}]^{0.5467}}\right]^2 = \frac{vD}{\nu}$$

Eq. 11

where v = pore velocity of fluid (m/s)

D = diameter of the cylinder (m)

ν = kinematic viscosity of fluid at temperature (m^2/s)

In keeping with the method developed by Perzlmaier et al. (2004), the effective Prandtl number in the above equation can be solved with:

$$Pr_{eff} = \frac{v}{k_{eff}} \qquad \text{Eq. 12}$$

where k_{eff} is the effective thermal diffusivity and can be taken as:

$$k_{eff} = \frac{\lambda_{eff}}{(\rho_{fl} \cdot c_{p\ fl})} \qquad \text{Eq. 13}$$

and λ_{eff} = effective thermal conductivity ($Wm^{-1}K^{-1}$)

ρ_{fl} = density of the fluid (kg/m^3)

$c_{p\,fl}$ = specific heat capacity of the fluid ($Jkg^{-1}K^{-1}$)

The reference value for kinematic viscosity of water at 12.5 °C is $1.32*10^{-6}$ m^2/s, the density of water is approximately 1000 kg/m^3, and the specific heat capacity is 4190 $Jkg^{-1}K^{-1}$. The effective thermal conductivity used was 1.4 $Wm^{-1}K^{-1}$, corresponding to the value of saturated Harps clay loam found by Ren et al. (2000). Lastly, the above equations can be rearranged to solve for pore velocity in the following manner:

$$v = \frac{v}{D} \cdot \left[\frac{\dfrac{D}{\left[\dfrac{\Delta T \cdot 2\pi}{q_L} - \dfrac{1}{\lambda_m} \cdot \ln\left(\dfrac{r_a}{r_i}\right)\right]\lambda_{fl}}}{1.248 \cdot Pr_{eff}{}^{0.3534} \cdot 1.325 \cdot \arctan[(D/d)^{0.5}]^{0.5467}} \right]^2 \qquad \text{Eq. 14}$$

To convert pore velocity to Darcy flux (which is helpful for considering infiltration) the pore velocity is multiplied by the soil porosity. For a silty clay loam the porosity is approximately 40%. Thus, Darcy flux equals 0.4 times the pore velocity.

4 Results

4.1 Full Scale Observations

A wetland water budget from 7/25 through 10/9/09 showed consistently decreasing infiltration rates over a wide range of values (see Figure 6). The greatest infiltration rates were observed at the beginning of the study in July, when calculated Darcy flux infiltration was 25 to 28 cm/d. Infiltration gradually decreased through August, despite increasing or comparable hydraulic head in the wetland (see Figure 7).

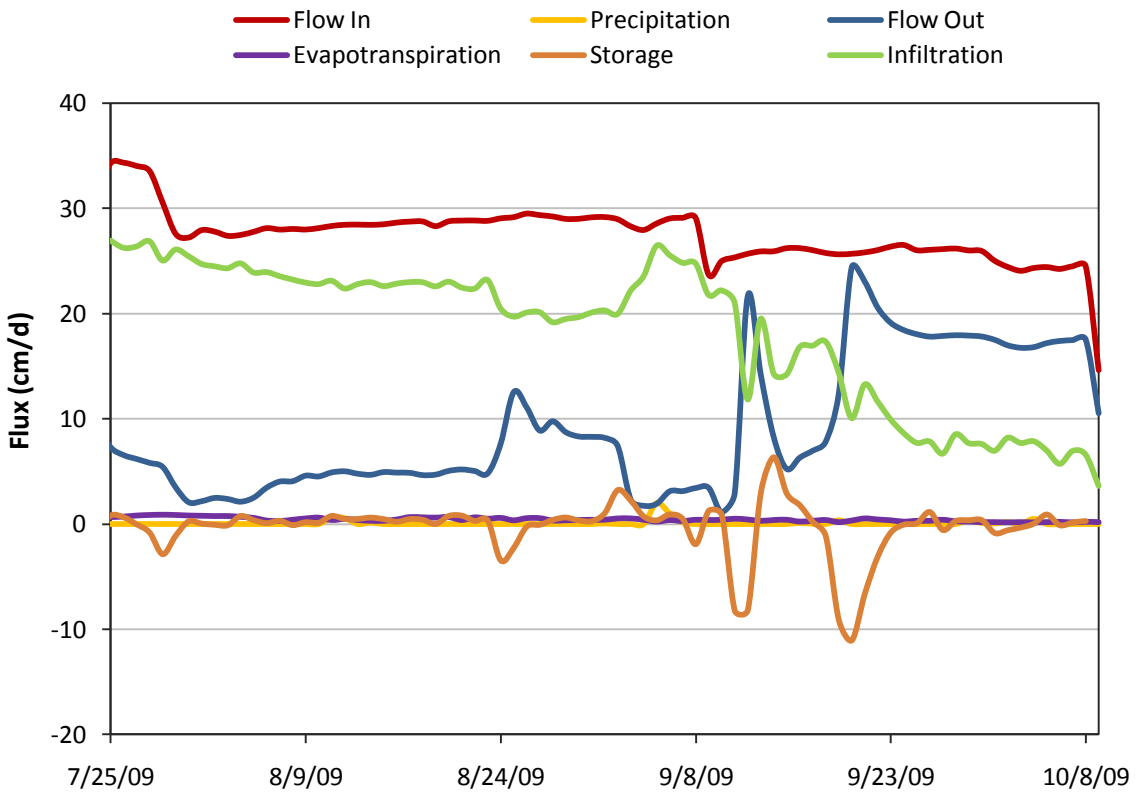

Figure 6 Components of the wetland water budget as fluxes (cm/d).

Changes in water level show some correlation with infiltration (e.g. the drop observed in Figure 7, 8/24 - 9/1) but do not ultimately overcome diminishing rates of infiltration through time. In mid-September, a substantial reduction of water depth, from 44 cm to 12 cm, significantly decreased infiltration from about 18 to 8 cm/d over a period of several days. For the duration of the study lasting through 10/9, water depth was maintained around 12 cm while infiltration showed a slightly negative trend, losing about 1 to 2 cm/d over that period.

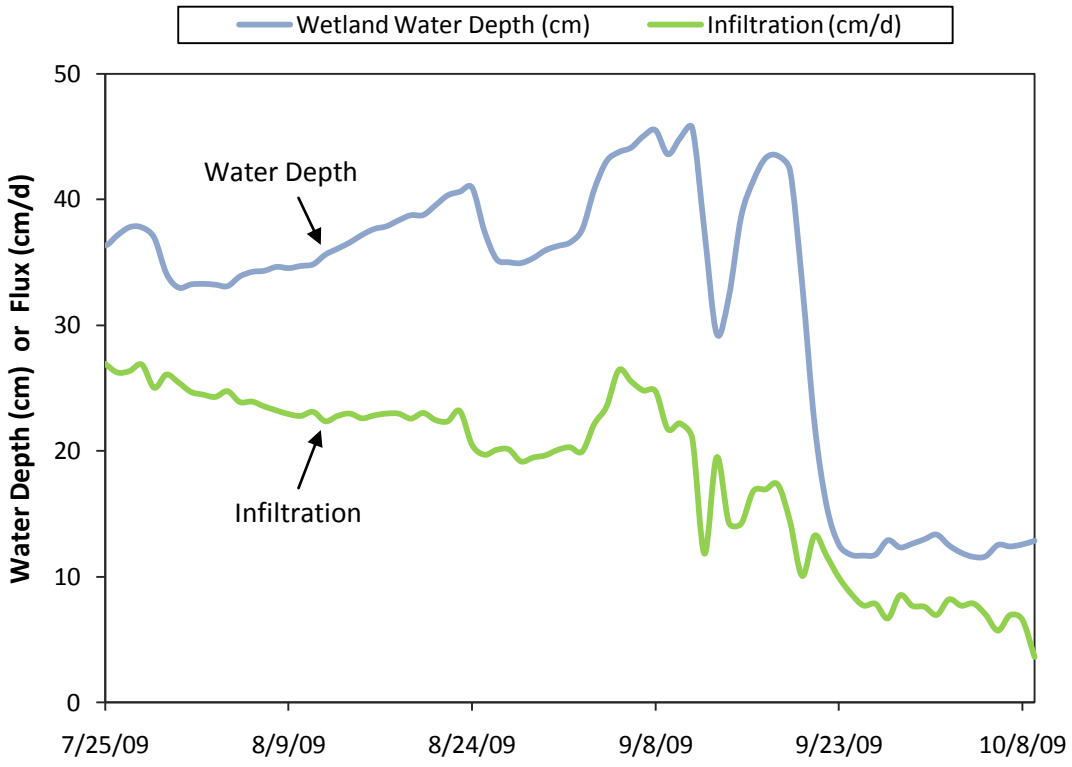

Figure 7 Infiltration rate and water depth during the summer/fall study period. Notice that the infiltration rate decreases through time, even while water depth increases (8/1-9/8).

Water level data obtained from pressure transducers in nearby piezometers indicated that decreasing infiltration in the wetland was not the product of water mounding in the shallow aquifer. Figure 8 shows the relationship between flow application through the wetland inlet and hydrologic response in the areas of Piezometer 2 (P2) and Piezometer 3 (P3) (see Figure 2.2 for locations of P2 and P3). In late June and early July, local water levels peaked indicating that water mounding is near a maximum, and thereafter declined through the rest of the study. If significant water mounding was occurring, the water infiltrating from the wetland would experience a decreased hydraulic gradient. However, the water table surrounding the wetland declines from July through October, which signifies that the hydraulic gradient from the wetland to the surrounding areas is actually increasing. Thus it is believed that water mounding is not responsible for observed decreases in wetland infiltration.

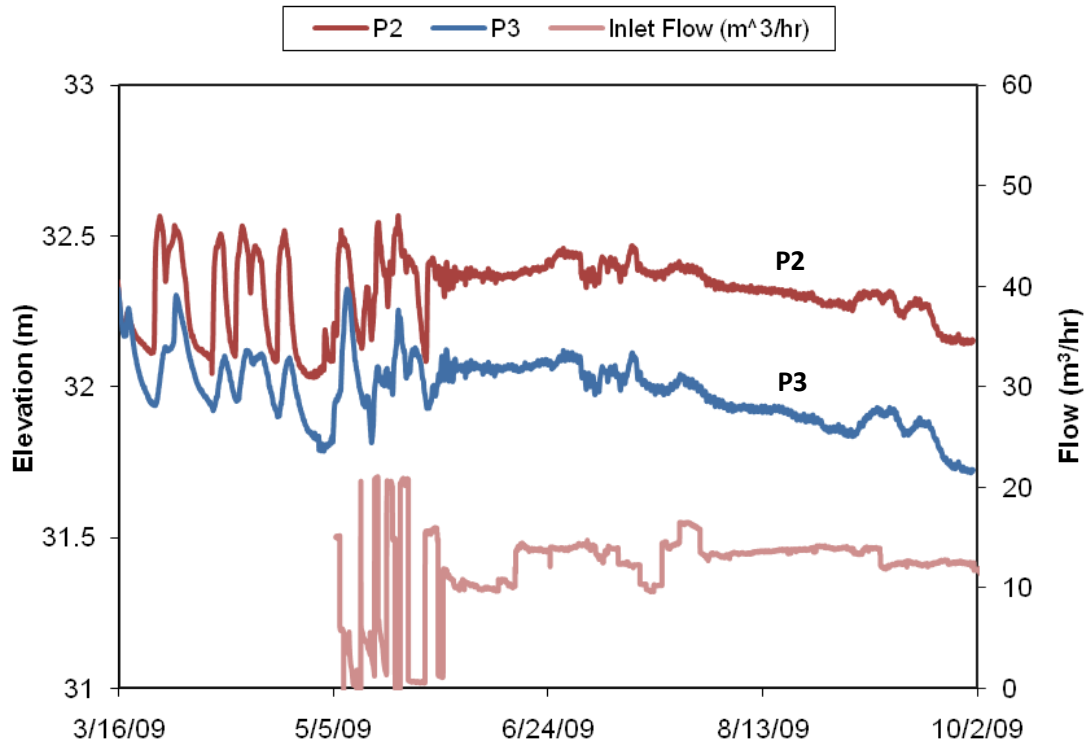

Figure 8 Water levels in two piezometers nearest the wetland and inlet flow rate. Notice that water levels peak in June and July and are decreasing August through September. Variability in P2 and P3 water levels prior to May are assumed to be related to precipitation and/or local flooding from the Pudding River.

Three suggestions have been devised to explain the observed decrease in wetland infiltration. First, the sudden reduction in infiltration that occurred in mid-September was likely due to decreasing the hydraulic gradient within the wetland, as well as a loss of lateral infiltration through the perimeter berms. The perimeter berms were responsible for keeping the water in the wetland. At higher water levels, these berms were submerged under 20 to 30 cm of hydraulic head and could potentially infiltrate substantial volumes of water in lateral directions with higher hydraulic gradients. When the water level in the wetland was reduced, as it was in mid-September by about 30 cm, the wetland lost a significant portion of this lateral infiltration, which contributed to the overall decrease in infiltration.

Secondly, most of the decrease in infiltration caused over the duration of the study may have been related to organic clogging in the soil horizon. According to Bouwer and Rice (1989) organic clogging layers commonly develop along the wetted perimeter of infiltration basins for artificial recharge. Bower and Rice noted that these clogging layers not only reduce the amount of infiltration that is expected with increasing water depth, but can actually cause

the rate of infiltration to decrease. Additionally, they observed that algae growth in such basins can form filter cakes on the basin bottom, which further decreases infiltration. These findings support the idea that organic clogging due to vegetative growth in the wetland throughout the summer and fall led to decreased permeability—and thus reduced infiltration—in the wetland soil. Significant algae growth observed throughout the wetland in July (see Appendix Figures C.11 and C.12) supports this theory.

Thirdly, it should be noted that Kadlec and Wallace (2008) have reported significant error in wetland water budgets and suggest using this method with caution. Therefore, a further possibility proposed here is that the decrease in infiltration was due to instrument drift in the inlet or outlet flow sensors (or both). Since the Magmeters reported expected accuracies of approximately ± 2%, instrument error is not considered likely. However, if the infiltration trends were attributable to error, drift in the inlet flow sensor seems most plausible since inlet flow rate was usually high and field observations were insufficient for validating sensor values. Yet error in either flow sensor—while considered unlikely—was possible.

4.2 Spatially Detailed Observations

DTS systems were used in conjunction with heated fiber optic cables to obtain information on the relative variability of infiltration. Figures 9 and 10 show the results of a 1-hour heat pulse taken in November 2008 with about 10 cm of standing water (see Appendix Figure C.10). In brief, substantial variability was not observed in any of the cable transects spanning the full longitudinal length of the wetland. Figure 9 shows the greatest range of relative variability observed, which differed by a factor of about two. Various spatial patterns can be observed in the cable transects, such as the high infiltration feature located at the midpoint of transect NEW and three distinct rises and drops in infiltration across transect NEW. For the most part, these features do not necessarily correspond to field observations except on a speculative level. Figure 10 shows the relative variability determined in the southern half of the wetland. While the average values were similar to the northern half, the greatest variability observed was well within a factor of two.

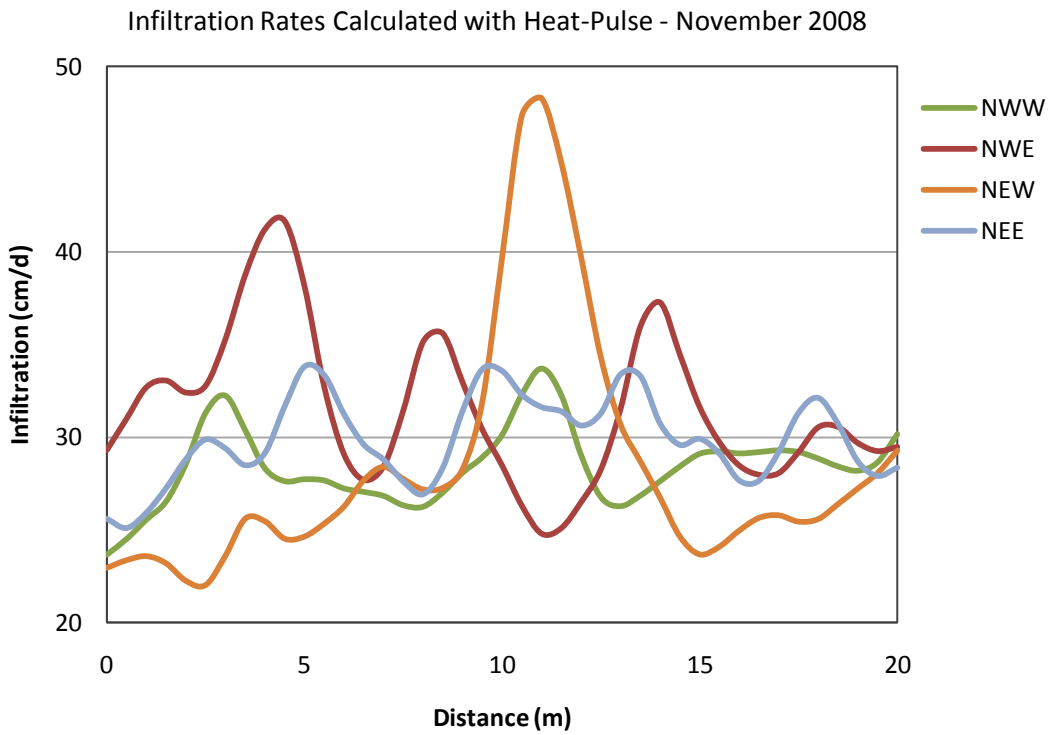

Figure 9 Relative variability of north wetland infiltration based on the thermal response of heated fiber optic cables. These data were collected in November of 2008 using a 1-hour heat pulse with about 10 cm of standing water in the wetland.

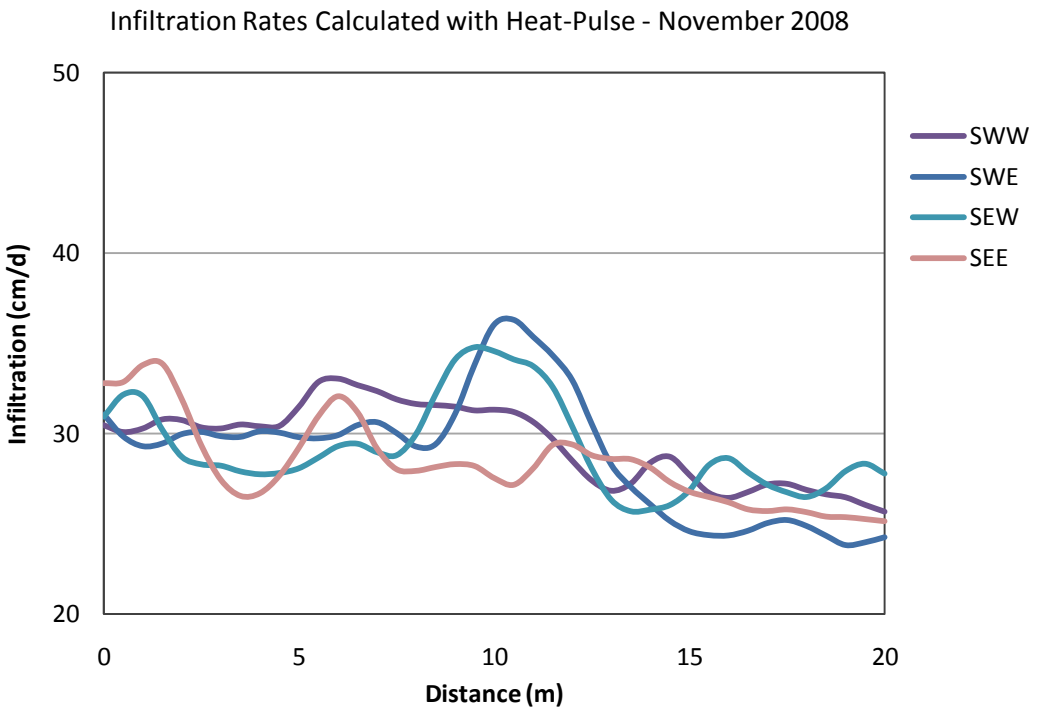

Figure 10 Relative variability of south wetland infiltration based on the thermal response of heated fiber optic cables. These data were collected in November of 2008 using a 1-hour heat pulse with about 10 cm of standing water in the wetland.

An additional 1-hour heat pulse was performed in June 2009 with about 15 cm of standing water. Figures 11 and 12 show the relative infiltrations in the north and south halves, respectively. The results from these graphs demonstrate that the average infiltration increased from November, while the variability decreased. It is suspected that the higher average infiltration is due to greater hydraulic head in the wetland during the June heat pulse—around 15cm, compared to about 10 cm in June. The decrease in variability suggests that the development of a soil clogging layer, changes in clay swelling, or additional settling within the wetland since the fiber optic installation might have occurred. The greatest range of variability observed from the June heat pulse ranged from 18 to 27 cm/d—or within a factor of 1.5.

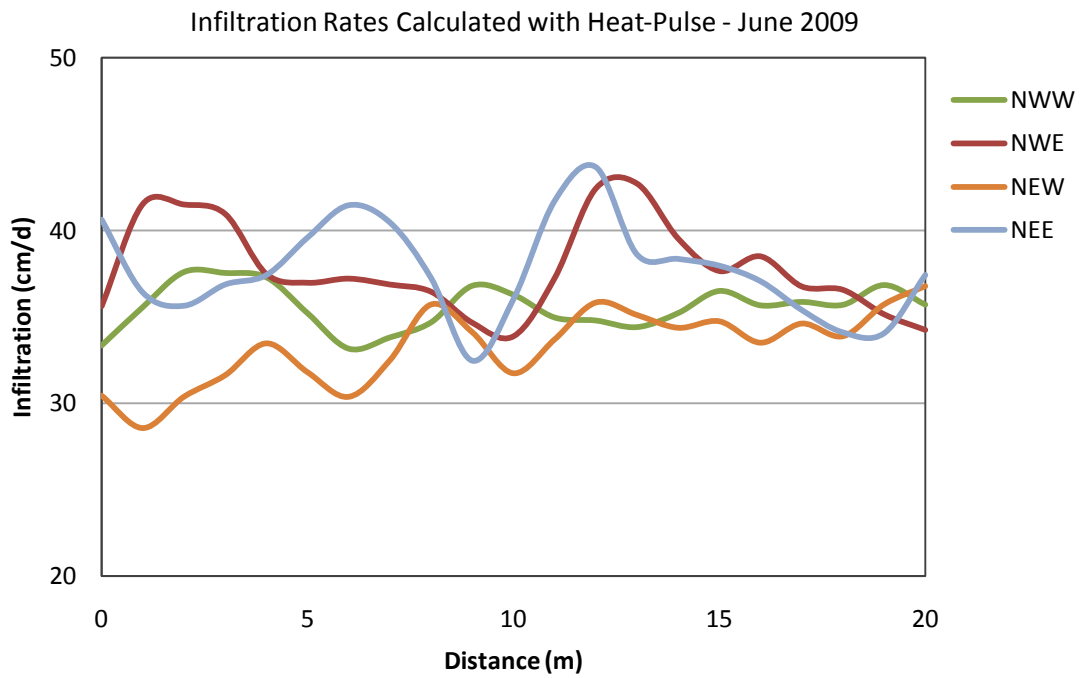

Figure 11 Relative variability of north wetland infiltration based on data collected in June of 2009 using a 1-hour heat pulse with about 15 cm of standing water.

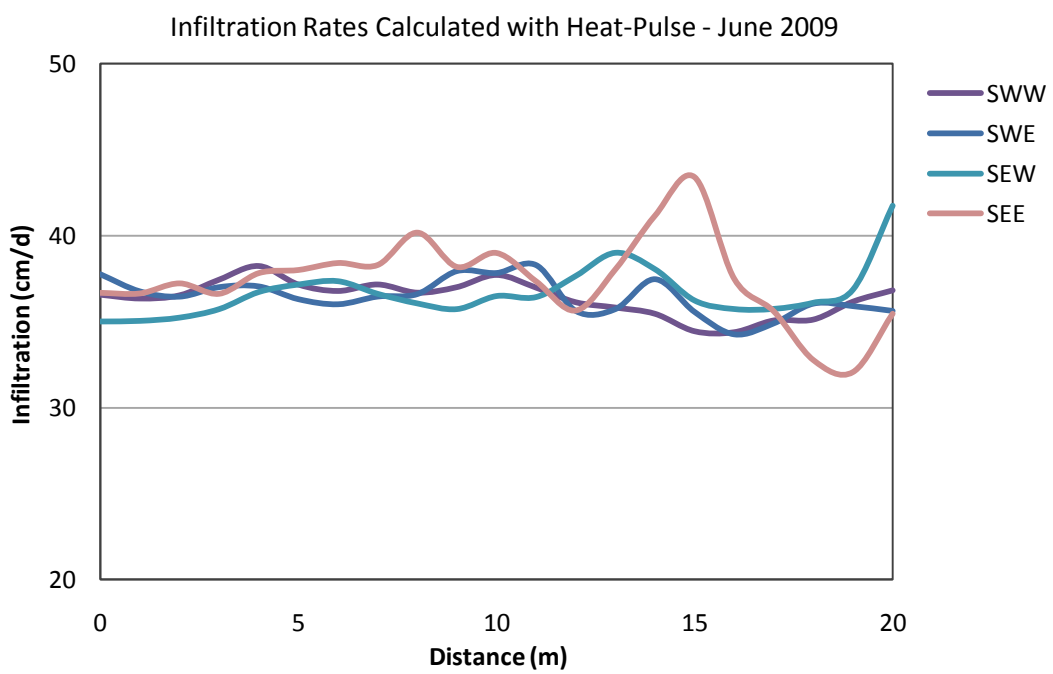

Figure 12 Relative variability of north wetland infiltration based on data collected in June of 2009 using a 1-hour heat pulse with about 15 cm of standing water.

5 Summary and Conclusions

The objective of this study was to characterize infiltration in the Woodburn WWTP pilot wetland during the summer and early fall of 2009. Based on a wetland water budget, Darcy flux infiltration ranged from around 18-28 cm/d when hydraulic head varied from 33 to 45 cm in late July through mid-September. When hydraulic head was reduced to 12 cm in late September through early October, infiltration was observed around 7-9 cm/d. Additionally, infiltration steadily decreased over the study duration, owing either to soil clogging, instrument error, or another unobserved process.

Spatial variability in infiltration determined with a DTS and buried fiber optic cables was not extreme, but within a factor of 2 for all heat pulse observations. Calculations of November 2008 and June 2009 heat pulses indicate that infiltration rates determined with identical procedures were comparable, but spatial variability decreased over that time—potentially due to soil settling, clay swelling or preferential clogging in zones of higher infiltration. The lack of variability observed in these heat pulses indicates that underlying drain tiles were not removing substantial quantities of water. This suggests that the drain tile plugging effort in 2008 was at least moderately effective.

In considering the use of these results for designing future treatment wetlands at the site, the wetland designer should be cautious for several reasons. First, the pilot wetland is relatively small in comparison to full-scale wetland expansion and heterogeneity in hydrogeology of the surrounding floodplain area could produce different results. Second, the period of research monitoring was relatively short (less than 3 months) and did not show infiltration behavior over several years, as would be occur with long-term treatment operations. Additionally, even in such a short monitoring period, the wetland exhibited a wide range of infiltration values depending on the hydraulic head and time of year (since infiltration was decreasing through the study). Fourth, relative infiltration variability was assessed in an area where drainage tiles had been unearthed and plugged in 2008. Whether the surrounding area is more or less variable will depend on where the wetland cells are located and on the effectiveness of underlying drain tiles.

6 Acknowledgements

We thank Jason Smesrud at CH2M HILL, the City of Woodburn, and Curtis Stultz, Jerry Tabler, Mike Arellano, Jordon Garner, and Ramon Garcia at Woodburn's Wastewater Treatment Plant.

7 References

Basinger, J.M., Kluitenberg G.J., Ham, J.M., Frank, J.M., Barnes, P.L., and M.B. Kirkham. 2003. Laboratory evaluation of the dual-probe heat-pulse method for measuring soil water content. Available at www.vadosezonejournal.org. Vadose Zone J. 2:389–399.

Blazejewski, R., and S. Murat-Blazejewska (1997) Soil clogging phenomena in constructed wetlands with subsurface flow, *Water Science and Technology* Vol. 35 (5), pp. 183–188.

Bouwer, H., and R.C. Rice (1989) Effect of Water Depth in Groundwater Recharge Basins on Infiltration. *Journal of Irrigation and Drainage Engineering* 115 (4), pp. 556-567.

Bristow, K. L., R. D. White, and G. J. Kluitenberg (1994) Comparison of single and dual probes for measuring soil thermal properties with transient heating, *Australian Journal of Soil Research,* Vol. 32, pp. 447-464.

Byrne, G.F., Drummond, J.E., and C.W. Rose. 1968. A sensor for water flux in soil. 2. "Line source" instrument. *Water Resour. Res.* Vol. 4, pp. 607-611.

Dakin, J. P., D. J. Pratt, G. W. Bibby, and J. Ross (1985) Distributed optical fiber Raman temperature sensor using a semiconductor light-source and detector, *Electron. Lett*., Vol. 21(13), pp. 569–570, doi:10.1049/el:19850402.

Fand, R. M., Varahasamy, M., and L. S. Greer (1993) Empirical correlation equations for heat transfer by forced convection from cylinders embedded in porous media that account for the wall effect and dispersion. *Int. J. Heat Mass Transfer,* Vol. 36 (18), pp. 4407 – 4418.

Healy, Robert P., and Mark F. Madison, CH2M HILL. Planning Document for the Selection of Temperature and Ammonia Reduction Alternatives. Rep. 2006. Print.

Hopmans, J.W., Bristow, K.L., and J. Simunek (2002) Indirect estimation of soil thermal properties and water flux from heat pulse measurements: Geometry and dispersion effects. *Water Resour. Res*. Vol 38

Johansson, S., and P. Sjödahl, "Downstream seepage detection using temperature measurements and visual inspection—monitoring experiences from Røsvatn field test dam and large embankment dams in Sweden," in Proc. Int. Seminar on stability and Breaching of Embankment Dams, Oslo, Norway, Oct. 2004, p. 21.

Kadlec, R.H., and S.D. Wallace (2008) Treatment Wetlands, second ed. CRC Press, Boca Raton, FL.

Knowles, P.R., Griffin, P., and P.A. Davies (2009) Complementary methods to investigate the development of clogging within a horizontal sub-surface flow tertiary treatment wetland, *Water Res.*, Vol. 44 (1), pp. 320-330.

Kurashima, T., T. Horiguchi, and M. Tateda (1990) Distributed-temperature sensing using stimulated Brillouin-scattering in optical silica fibers, *Opt. Lett*., Vol. 15 (18), pp. 1038–1040.

Langergraber, G., Haberl, R., Laber, J. and A. Pressl (2003) Evaluation of substrate clogging processes in vertical flow constructed wetlands. *Water Sci. Technol.* Vol. 48 (5), pp. 25–34.

Mori, Y., Hopmans, J. W., Mortensen, A. P., and G.J. Kluitenberg (2003) Multi-Functional Heat Pulse Probe for the Simultaneous Measurement of Soil Water Content, Solute Concentration, and Heat Transport Parameters, *Vadose Zone J.*, Vol. 2(4), pp. 561-571.

Mori, Y., Hopmans, J. W., Mortensen, A. P., and G.J. Kluitenberg (2005) Estimation of Vadose Zone Water Flux from Multi-Functional Heat Pulse Probe Measurements, *Soil Sci. Soc. Am. J.*, Vol. 69(3), pp. 599-606.

Muñoz-Carpena, R., and J. E. Parsons (2000) VFSMOD, v.1.04, User's Manual. Raleigh, NC: North Carolina State University.

Perzlmaier, S., Aufleger, M., and M. Conrad (2004) Distributed Fiber Optic Temperature Measurements in Hydraulic Engineering—Prospects of the Heat-up Method. Proceedings of the 72nd Annual Meeting of the International Commission on Large Dams (ICOLD), Seoul, Korea, 16.-22.05. 2004, p.31.

Perzlmaier, S., Strasser, K. H., Strobl, T., Aufleger, M. (2006) Integral Seepage Monitoring on Open Channel Embankment Dams by the DFOT Heat Pulse Method. Proceedings of the 22nd Congress of the International Commission on Large Dams (ICOLD), Barcelona, Spain, Q. 86 – R12, p. 145 – 164.

Ren, T., Kluitenberg, G. J., and R. Horton (2000) Determining soil water flux and pore water velocity by a heat pulse technique, *Soil Sci. Soc. Am. J*., Vol. 64, pp. 552 – 560.

Sayde, C., Gregory, C., Rodriguez, M., Tufillaro, N., Tyler, S., Van de Giesen, N., English, M., Cuenca, R., and J. Selker. Feasibility of soil moisture monitoring with fiber optics. In Review. *Water Resources Res.*

Selker, J.S., The´venaz, L., Huwald, H., Mallet, A., Luxemburg, W., Van de Giesen, N., Stejskal, M., Zeman, J., Westhoff, M., and M.B. Parlange (2006) Distributed fiber-optic temperature sensing for hydrologic systems. *Water Resour. Res.*, Vol. 42: W12202.

Tarara, J. M., and J. M. Ham (1997) Measuring soil water content in the laboratory and field with dual-probe heat-capacity sensors. *Agronomy Journal*, Vol. 89, pp. 535-542.

Van Cuyk S., Siegrist, R., Logan, A., Masson, S., Fischer, E., and L. Figueroa (2001) Hydraulic and purification behaviors and their interactions during wastewater treatment in soil infiltration systems, *Wat. Res.*, Vol. 35(4), pp. 953-964.

Wagner, W. (1998) Wärmeübertragung, Grundlagen, 5., überarbeitete Auflage. Vogel Buchverlag, Würzburg.

Wang, Q., Ochsner, T.E., and R. Horton (2002) Mathematical analysis of heat pulse signals for soil water flux determination, *Water Resour. Res.*, Vol. 38(6).

Weiss, J.D. (2003) Using fiber optics to detect moisture intrusion into a landfill cap consisting of a vegetative soil barrier, *Journal of the Air and Waste Management Assoc.* Vol. 53, pp. 1130–1148.

Appendix 3: Detecting Groundwater Inflows and Hyporheic Discharge through DTS Temperature Analysis for Restoration Monitoring

Detecting Groundwater Inflows and Hyporheic Discharge through DTS Temperature Analysis for Restoration Monitoring

From the OSU MS Thesis of Julie Huff, 2009

Introduction

Watershed health is becoming a large industry in the Pacific Northwest. From 1999-2008 over $680 million was spent on salmon recovery on the Pacific coast (NOAA, 2009) and, on average, over $1 billion was spent annually on river restoration in the nation (Bernhardt et al., 2005). Restoring salmon habitat is the main objective for watershed funds used in Oregon. Much of the historical salmon habitat in Oregon was negatively affected due to anthropogenic activities occurring in the past 150 yrs. For example, miles of habitat for migrating fish have been blocked off by dams, mining and splash dams have altered the channel geometry and bed material, and grazing and logging have greatly decreased the amount of riparian vegetation around the streams and rivers. The effects of human activity have caused the salmon population to plunge to roughly six percent of historical numbers within the Columbia River basin (McCullough, 1999). To revitalize the salmon population, restoration efforts have focused on in-stream habitat improvement, riparian vegetation management, fish passage and water quality management (Taylor, 2007).

To be effective, restoration practices should be designed to permanently re-establish degraded or lost processes and not just provide a band-aid to give short-term improvement. This leads to two questions: 1) exactly which processes should be focused on? And, 2) how do you restore these processes? The EPA Clean Water Act has listed temperature, oxygen depletion, and sediment as three of the top five quality impairments of waterways within Oregon (US EPA, 2006). For example, to decrease temperature, should riparian vegetation be planted, or should the sinuosity be increased to promote hyporheic exchange? Are all secondary effects of restoration practices known? For example, improving salmonid habitat is the main objective for using engineered log jams, but recent studies show hyporheic exchange as another effect of in-stream structures (Hester and Doyle, 2008; Crispell et al., 2009). These questions will not be answered within this study, but are the motivation for the study, which is to monitor the temperature effects of restoration and determine what processes, if any, have been altered.

Monitoring of restoration is underfunded and underutilized in the US with only 10% of projects being monitored or evaluated (Wohl et al., 2005; Bernhardt et al., 2005), although its importance is being recognized more and more with books such as Roni and Quimby's *Monitoring Stream and Watershed Restoration* and Wohl's (2005) review of the subject. Yet, it's unfortunate that Roni and Quimby don't address temperature when it is such an important factor in salmonid heath. For temperature modeling there are a handful of strategies ranging from simple, such as recording temperature year after year, to complex, such as modeling the river using a process

based temperature model (Independent Scientific Advisory Board, 2003). Monitoring data should be a tool for adaptive management and scientific advancement; therefore, a physically based temperature model calibrated with high resolution data, such as forward looking infrared thermal imaging (FLIR) or distributed temperature sensing (DTS), is an excellent strategy (Torgersen et al., 2001; Westhoff et al., 2007). Unfortunately this modeling strategy is very consuming in both time and money; therefore the objective of this study is to determine what cooling processes can be identified with only high resolution data from DTS technology.

The use of DTS and fiber optics to measure temperature was introduced to the ecological field in 2006 (Selker et al., 2006b). It excels in acquiring high resolution temperature data both temporally and spatially with time and distance steps on the order of 30 sec and 1m, respectively (Tufillaro et al., 2008). The DTS system has been used to determine points of groundwater inflow in headwater streams (Selker et al., 2006a), to observe cool air drainage in mountain valleys (J. S. Selker et al., 2008) and to watch the building and melting of snowpacks (Tyler et al., 2009). DTS is a powerful tool that, when paired with statistical analysis like the work of Arrigoni et al. (2008), can provide a new look into how rivers work.

Temperature Signature

Riparian vegetation lowers the incidence of solar radiation, the main driver of peak river temperatures, but as the width of the river increases, the efficacy of riparian shading decreases. In reaches without riparian vegetation, or in larger rivers, the groundwater inflows and hyporheic exchange become more important in lowering peak summer temperatures. Groundwater inflow consists of areas on the streambed where there is direct or diffuse inflow from a groundwater source. The distinction between groundwater and hyporheic flows is controversial and somewhat subjective, but here the thermally-based definition of a groundwater: a source of lateral inflow with a temperature that is largely constant on a daily time-scale (potentially variable seasonally). In particular, groundwater inflow will be lower in temperature than the summer river temperature due to residence times of months to years. The temperature signal seen at areas of groundwater inflows will have an overall cooling effect in summer, both during the day and night (Arrigoni et al., 2008).

Hyporheic exchange is defined here as areas where surface water leaves the channel (hyporheic recharge) and enters the subsurface material (hyporheic zone). In the hyporheic zone, water typically changes both its temperature and chemical signature. After emerging from the hyporheic zone, the water re-enters the stream (hyporheic discharge) further downstream from where it entered. The distance the hyporheic water travels, the new temperature, and chemical signature depend on the particular flow path and are highly variable. This flow path is driven by hydraulic gradient, hydraulic conductivity and the topography of streambed and floodplain (Arrigoni et al., 2008; Gooseff et al., 2006; Wondzell, 2006; Wondzell et al., 2007).

The temperature of hyporheic discharge varies depending on the length and depth of the flow path; a longer flow path typically means a longer residence time. Since the hyporheic zone in general involves shorter residence times than groundwater (hours to days), averaging diurnal temperatures rather than carrying seasonal history, the hyporheic discharge will be cooler than surface water during the day and warmer than surface water in the evening (e.g. Figure 3.1, Collier, 2008). In addition, streamlines of hyporheic and groundwater cannot cross therefore there is no groundwater mixing with hyporheic water in the hyporheic zone. Areas of groundwater inflow and hyporheic discharge cannot occur simultaneously (Figure 3.2).

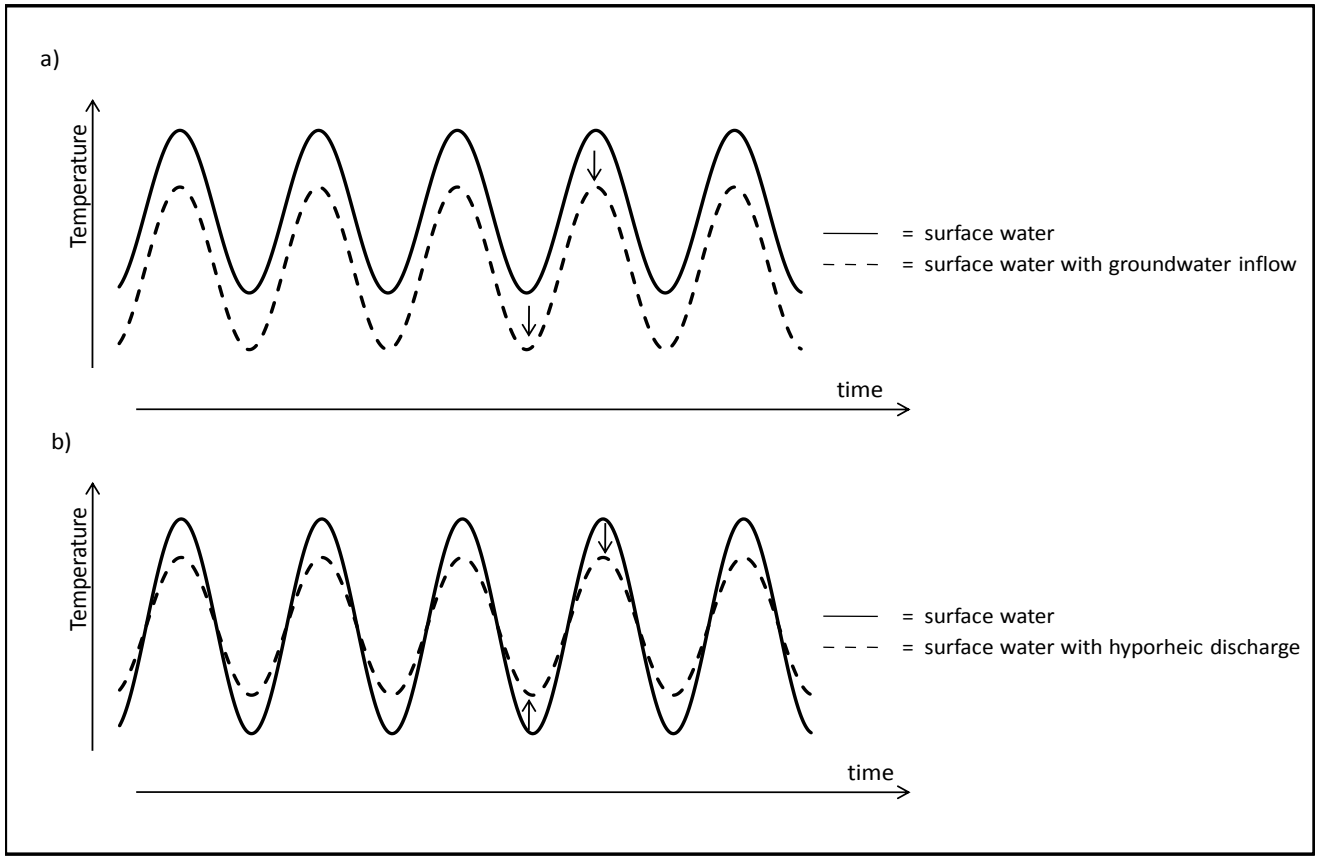

Figure 3.1 A conceptual model of how temperature of surface water reacts to the mixing of a) groundwater inflows and b) hyporheic exchange during baseflows of summer.

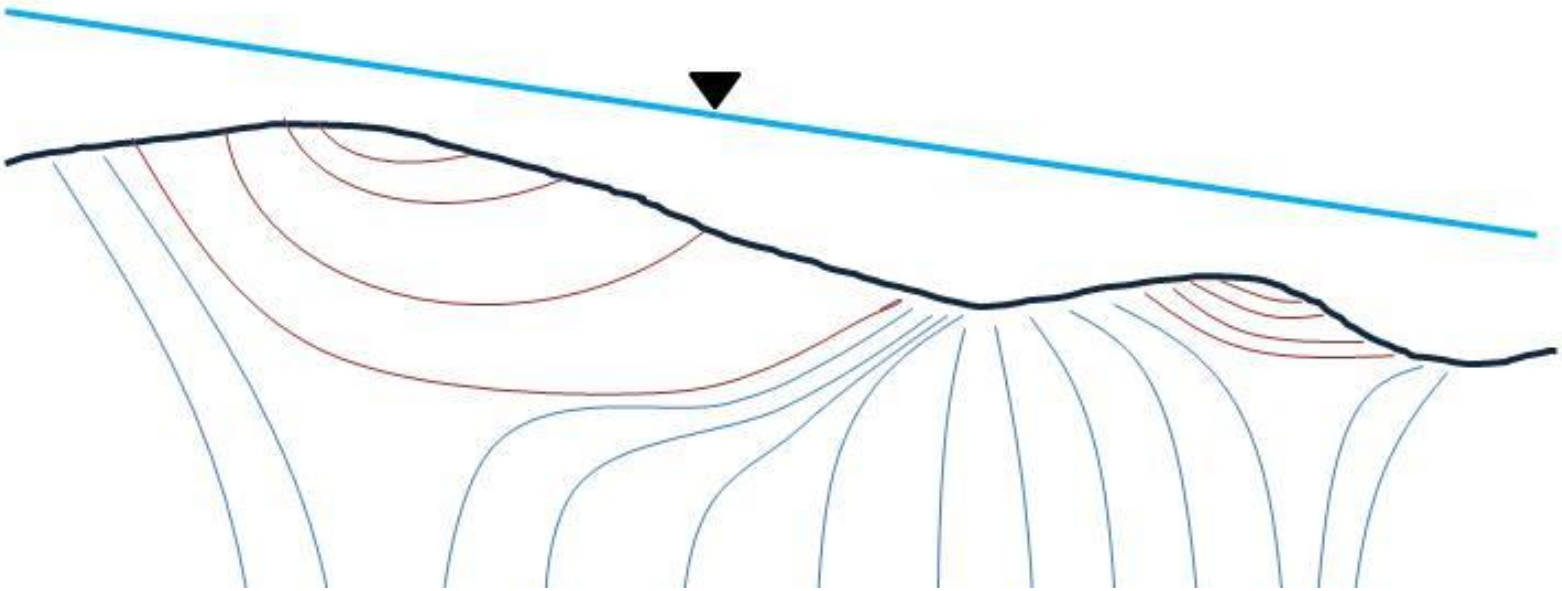

Figure 3.2 A conceptual model of subsurface streamlines below a river viewed as a longitudinal cross-section. The red streamlines represent hyporheic flow while the blue streamlines represent groundwater flow. Streamlines do not converge therefore groundwater and hyporheic discharge occurs at different locations.

We seek to detect and quantify the temperature signatures of groundwater inflow and hyporheic discharge along the course of a river. Traditional point measurements of temperature are not conducive to locating areas of groundwater and hyporheic discharge. FLIR, a newer technology, gives higher spatial resolution than DTS data but is costly to carry-out, and thus involves only 2 or 3 temporal snap shots of the top-surface of a river. The low temporal resolution and inability to penetrate the surface creates difficulty in distinguishing groundwater inflows from hyporheic discharge within the river. The DTS provides excellent resolution, both temporally and spatially, and measures directly on the stream bed, making it the optimum technology for temperature measurements used to identify groundwater inflows and hyporheic exchange.

Methods

Site Description

For a full site description see Chapter 2: Site Description. The first phase of the restoration design for the Forrest property was completed during the in-stream work window of July 14th to Aug 14th, 2008. During this time period, 33 rock barbs were removed from the stream channel. At some of the locations, rock barbs were replaced with engineered log jams (ELJs). A total of 17 ELJs were installed ranging from small structures to large multi-log structures with scour pools dug out around 12 of the 17 ELJ structures. The objective of the restoration was to increase habitat for both adult and juvenile salmonids by adding ELJs. The 2008 results indicate an increased use of the ELJ scour pools by salmonids following treatment (Table 3.1) (Turo, 2009). Although the salmonid use of the scour pools increased, we seek to discover if the temperature profile changed. Did the use of the scour pools increase due to the slower velocities and cover of the ELJ or did the temperature characteristic of the site change, thus drawing more fish?

Table 3.1 Fish use of the study site before and after restoration (Turo, 2009)

	Aug 29, 2006 - All pools in restoration reach	Aug 1, 2008 - 17 constructed ELJ sites
Chinook salmon parr	13	39
Steelhead/trout parr (<6")	9	28
Redband trout (>6")	4	10

The motivation behind restoration of the Forrest reach is lack of habitat complexity created by the unnatural rock barbs. Although the rock barbs lack habitat complexity maybe they provide unknown benefits to the river. Increased hydraulic

gradients due to in-stream structures, such as rock barbs or ELJs, can induce hyporheic exchange providing cool thermal refugia (Hester et al., 2009). The addition of ELJs are to increase habitat complexity and depending on their placement during low flow they could create a secondary effect and promote hyporheic exchange (Crispell et al., 2009; Hester et al., 2009; Hester and Doyle, 2008). Rivers are a conglomerate of complex processes that are difficult to predict, monitoring of restoration can be a great learning tool for new insights into river processes.

Field Measurements and Instrumentation

This study utilized the high resolution temperature data that DTS technology produces. An Agilent N4386A instrument was used with a pair of two kilometers fiber optic cables. The two cables were placed in the river about1meter from each bank and recorded temperatures every 10 minutes with one meter spatial resolution. For a more detailed account of how the DTS was installed see Chapter 2: Field Measurements and Instrumentation.

Analysis

Here we build on the calibration and processing work presented in Chapter 2 to employ these prepared data specifically to quantify stream-subsurface interactions.

Groundwater inflow and Hyporheic Exchange Identification

In our framework, groundwater has a distinct temperature signal that is nearly constant year-round and, absent flow to very great depths or contact with geothermal heat sources, can often be assumed to equal the average annual air temperature (Anderson, 2005). When groundwater emerges into surface water, it can produce a cooling effect during high summer-time temperatures or a warming effect during cold winter temperatures. The groundwater will have the greatest effect on surface water temperature during a combination of large temperature differences and low stream flow; this tends to occur in the late summer. The amount of groundwater entering a stream is not constant and depends on the hydraulic gradient of the groundwater table to the stream. During winter there is a steeper hydraulic gradient due to higher groundwater tables. Figure 3.1 demonstrates how cold groundwater affects summer temperatures, both during the day and at night.

The temperature signal of hyporheic exchange is dependent on residence time and its flow path through the hyporheic zone. Both the residence time and flow path reflect local river characteristics, mainly topography and the hydraulic conductivity of the streambed (Arrigoni et al., 2008; Gooseff et al., 2006; S. M Wondzell, 2006; S. M Wondzell et al., 2007). Due to the timing of the start of this study, we must compare data that span some significant changes in river stage. The pre-restoration analysis was completed in early July 2008 when the flows were

abnormally high. Typically, temperature signals are weakened during high flows because the diurnal temperature range and the ratio of hyporheic to surface water are smaller. Luckily in this case, even with the high flows, the diurnal water temperature range was still large due to a heat wave, fluctuating at most 10 °C from day to night. The post-restoration analysis was done in late August 2008 to early September 2008 and had flows a third to a half as large as pre-restoration analysis. Similar to pre-restoration conditions, the diurnal water temperature range was up to 10°C. The main differences between pre- and post-restoration conditions are air temperature, surface water flow and groundwater height. There is conflicting evidence in literature whether hyporheic exchange increases or decreases during higher flows (S. M Wondzell, 2006). If hyporheic discharge has the largest signal during the months of higher daily peak temperatures and is not influenced by the change in flow, comparison of pre- and post-restoration is possible.

It is our hypothesis that analysis of the DTS temperature profile of the Forrest property can identify locations of distinct temporal patterns that are associated with groundwater inflows and hyporheic discharge. In this study the term “profile” means a temperature fluctuation with distance along the river. The identified areas will be located at one meter resolution. A key assumption is that both groundwater and hyporheic discharge create localized temperature differences large enough to be detected by the DTS. To aid in detection of signals, the fiber optic cable is placed directly on the streambed. Therefore, when the cooler or warmer water emerges from the subsurface the DTS will register the temperature before it becomes fully mixed within the river. Temperature profiles of the river should be sufficient to identify areas whose temperatures are significantly different upstream and downstream. A conceptual model of these localized temperature differences using the DTS data is presented in Figure 3.3, illustrating three strategies to quantify spatial changes in temperature.

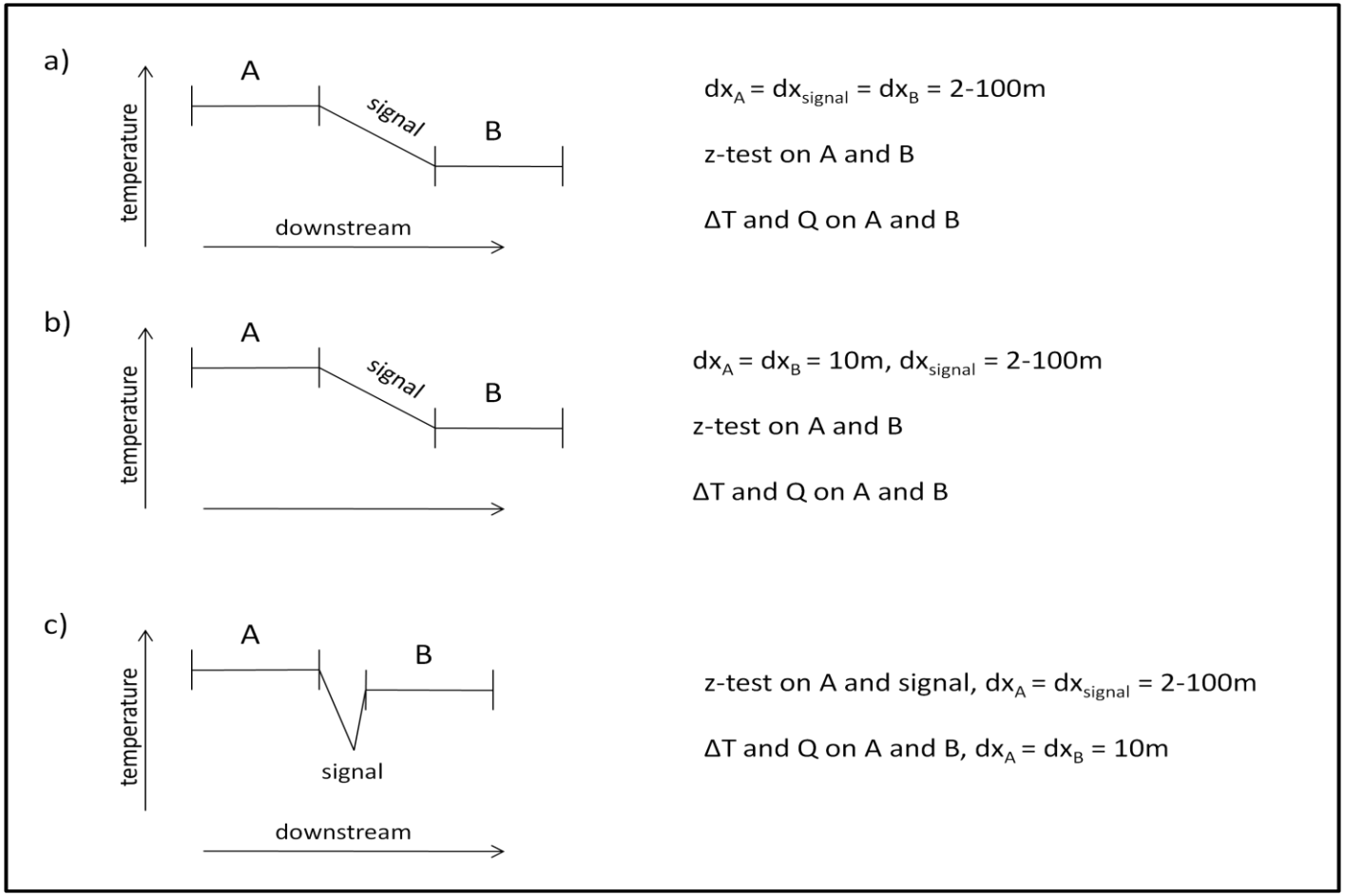

Figure 3.3 Summary of the 3 different strategies used to determine signal locations.

This thesis focuses on identifying the effects of river restoration on stream-subsurface interactions by comparing computed groundwater inflow and hyporheic discharge from before and after restoration. The pre-restoration analysis will also give some insight as to how these two processes change with higher flows for the Middle Fork of the John Day River (MFJD). A statistical analysis of the temperature profile during the hottest four hours and coldest four hours of each day will be utilized.

To obtain a data set with the required temporal resolution, each data set, river right (RR) and river left (RL) of pre-restoration (pre) and post-restoration (post), was temporally averaged using a 60 minute moving average filter. This minimized the noise seen within the data which were collected every 10 minutes. This is a standard technique in DTS data collection wherein the basic computation is one of photon counting, so the instrument is set to the highest temporal resolution one can envision needing, and lower resolution higher precision data is then obtained by post-processing to obtain the specific temporal resolution required. The same analysis was used for all four data sets but the following description will be only for RL-post (Aug 28 -Sept 3 2008). The hottest four hours of the water temperature for RL-post were averaged for every meter of cable within the river, resulting in six temperature profiles. These profiles of the hottest water temperature will be referred to as “Hot”. The same was done with the four coolest hours of water temperature and will be referred to as “Cold”. The hours associated with Hot and Cold are 3:00-7:00 pm and 5:30-9:30 am, respectively.

The following analysis uses the Hot and Cold profiles to determine if there are areas, referred to as signals, with temperatures that are significantly different from areas directly upstream and downstream. The two common types of signals that occur from groundwater inflows and hyporheic discharge are a gradual change in temperature and an abrupt change in temperature. The gradual change in temperature can be associated with a diffuse groundwater inflow and would typically be found in the fully mixed surface water. The second signal is a distinct localized change in temperature that could be caused by direct groundwater inflows. The signal length of groundwater or hyporheic can range anywhere from less than a meter to over hundreds of meters (G. C. Poole et al., 2008). Therefore, analysis was completed to identify signals at 11 different lengths: 2, 4, 6, 10, 16, 20, 30, 40, 60, 80 and 100 meters.

Three different strategies could be used to compare the change in temperature of these two signals. First, the upstream (US) could be compared to the downstream (DS) with US and DS having the same lengths as the signal. Through visual inspection this method misses signals that have a distinct spike but a small overall change in temperature from US to DS. Also when the signal length becomes large (100m) this strategy misses the upstream and downstream 150m of the reach.

The second strategy is similar to the first but instead, uses lengths of 10m for US and DS. Again, through visual inspection the temperature spikes are missed. Even though the spikes do not create a large temperature difference in the overall reach they are important because they provide localized thermal refugia for fish during peak summer temperatures. The third strategy compares the signal with US, where the US and signal have a length of 2-100m. Then overall temperature change is calculated between the US and DS, both with lengths of 10m. Although this method misses the upstream and downstream 100m it does not miss the spikes seen within the profile and therefore it was chosen for use in our analysis. In addition, the cable is in direct contact with the river sediment therefore it will measure the discharge temperature before it has been fully mixed with the surface water causing a localized change in temperature. A summary of these three strategies can be found in Figure 3.3.

To determine whether or not the signal had a significantly different mean than the upstream section, a z-test was used ("Hypothesis Test Assumptions," 2009). The z-test was chosen over a t-test to compare the mean temperature because the measurement error (standard deviation) of the dataset is known. The difference in temperature was significantly different if the ΔT was larger than the noise of the data set. The following analysis was done for every signal length from 2-100m and a signal length of 6m will be used for the example calculations. The standard deviation of the noise was calculated for RL-post with no averaging in Chapter 2: Data Analysis. The standard deviation used for this analysis will be different because the data set was averaged using a 60 minute moving average and then averaged again to get the Hot and Cold temperatures. Therefore, equation (3.1) was used to determine the new standard deviation of the dataset, σ_{mav} .

$$\sigma_{mav} = \frac{\sigma}{\sqrt{N}} \tag{3.1}$$

where σ is the standard deviation of the noise and N is the number of data points used to average. N is calculated using equation (3.2).

$$N = signal\ length \cdot (30) \tag{3.2}$$

where signal length is in meters. The number 30 is derived by adding the six data points from the moving average and the 24 data points from the four hottest or coldest hours of the day.

The z-test tests the null hypothesis that the mean of the signal with standard deviation, σ_{mav} , is equal to the mean of the upstream section against the alternative that that the two are not equal. The z-test was performed at the 1% significance level and was run on all 12 Hot and Cold temperature profiles. A groundwater inflow was identified when the temperature of the signal was cooler than the upstream temperature during the Hot and Cold profile of all 6 days. A hyporheic discharge signal was identified when the temperature of the signal was cooler than the US

temperature during the Hot profile but warmer than US during the Cold profile. This analysis was performed for every signal length from 2-100m.

The results of the analysis gave overlapping signal lengths at every groundwater inflow and hyporheic discharge location. The signal length that corresponds with the greatest temperature difference was selected as the correct signal length. This will prevent a large temperature difference from being identified as a 100m signal when it is actually only a 16m signal. The greatest temperature difference is expressed as the sum of the absolute temperature difference between the upstream and signal temperatures for all 12 Hot and Cold profiles.

Visual comparison of groundwater and hyporheic locations was completed using photographs and LiDAR of the study reach. The photographs were taken during documentation of the cable installation and are spaced out every 20 to 50m. The LiDAR was completed in 2006 by the firm Watershed Sciences and overlaid onto a Google Earth image of the site. The results of the groundwater and hyporheic analysis were also added to the Google Earth image for easy visual comparison.

Groundwater Inflow Quantification

The quantity of groundwater inflow can be established by applying the mass and energy conservation equations of Kobayashi (1985). This assumes that the entire temperature difference from above and below the groundwater inflow is due solely to the emergence of groundwater.

Mass Balance: $Q_d = Q_u + Q_g$ (3.3)

Energy Balance: $T_d Q_d = T_u Q_u + T_g Q_g$ (3.4)

where Q is flow (m^3/s), T is temperature (°C) and d, u and g stand for downstream flow, upstream flow and groundwater flow, respectively. The mass and energy balance can be solved because there are two equations and two unknowns, Q_d and Q_g, giving equation (3.5).

$$Q_g = Q_u \left(\frac{T_u - T_d}{T_d - T_g}\right) \quad (3.5)$$

These equations are correct when the groundwater inflow is large enough to influence the temperature of the mixed river. The flow was calculated at all groundwater inflow signals for the six Hot and six Cold periods. The 12 flows are then averaged together and distributed across the signal length equally.

Results

Groundwater inflow and Hyporheic Exchange Identification

The 60 minute moving-average performed on all data sets greatly minimized the noise seen in the data (Figure 3.4). The Hot and Cold profiles were calculated giving 20 temperature profiles for pre-restoration and 12 temperature profiles for post-restoration. By visual inspection, multiple areas along the temperature profile

can be seen in which temperature decreases during both Hot and Cold time periods (Figure 3.5). To strengthen the analysis beyond visual inspection, a statistical analysis was performed. The following results will focus on the river left post-restoration data set and the lengths of river 205-225m and 315-335m to demonstrate areas of groundwater inflow and hyporheic discharge, see Figure 3.6.

The standard deviation of the measurement noise was calculated using the ice baths as outlined in Chapter 2: Data Analysis and can be found in Table 3.2. For RL-post the standard deviation of noise for each signal length analysis can be found in Table 3.3.

For each signal length and temperature profile, a z-test was performed on the temperature of the signal and the temperature directly upstream. This amounts to 132 z-tests for each meter of cable with the lengths of both the signal and the upstream section being equal. The difference in mean temperature of the upstream segment compared to the signal used for the z-test can be found in Table 3.4 for meters 205-225 and Table 3.5 for meters 315-335. The z-test results for the meters above can be found in Table 3.6 and Table 3.7.

Table 3.2 standard deviation of measurement noise for each DTS data set. The measurement noise was calculated for the hours of complete ice bath where the temperature was assumed to be 0 °C.

	Standard Deviation (°C)
Pre-RL	0.253
Pre-RR	0.458
Post-RL	0.376
Post-RR	0.421

Table 3.3 Standard deviation of measurement noise in the river left post-restoration data for different signal length analyses. The standard deviation decreases with increasing signal length because the number of data points used for averaging increases with signal length.

Signal Length (m)	Std Dev (°C)
2	0.033
4	0.023
6	0.019
10	0.015
16	0.012
20	0.010
30	0.008
40	0.007
60	0.006
80	0.005
100	0.005

Table 3.4 The calculated difference in mean temperature of the signal and the upstream section for the 6 Hot and 6 Cold temperature profiles at a signal length analysis of 2m. The values in bold represent possible groundwater inflows because the signal is colder than the upstream section for the 12 profiles.

	Distance Downstream of Signal Length (m)										
	215	216	217	218	219	220	221	222	223	224	225
Hot Day 1	-0.015	*-0.011*	0.007	**-0.068**	**-0.266**	**-0.346**	**-0.346**	**-0.170**	0.271	0.441	0.408
Hot Day 2	-0.033	*-0.033*	-0.013	**-0.040**	**-0.151**	**-0.209**	**-0.204**	**-0.091**	0.171	0.280	0.250
Hot Day 3	-0.028	*-0.028*	-0.022	**-0.122**	**-0.394**	**-0.497**	**-0.479**	**-0.249**	0.333	0.555	0.527
Hot Day 4	-0.052	*-0.041*	-0.006	**-0.119**	**-0.570**	**-0.737**	**-0.740**	**-0.460**	0.479	0.821	0.783
Hot Day 5	-0.042	*-0.054*	-0.041	**-0.108**	**-0.329**	**-0.415**	**-0.393**	**-0.185**	0.321	0.520	0.478
Hot Day 6	-0.043	*-0.033*	-0.012	**-0.049**	**-0.155**	**-0.206**	**-0.198**	**-0.087**	0.150	0.258	0.243
Cold Day 1	-0.051	*-0.039*	-0.009	**-0.086**	**-0.364**	**-0.492**	**-0.507**	**-0.304**	0.288	0.547	0.546
Cold Day 2	-0.019	*-0.023*	-0.017	**-0.107**	**-0.376**	**-0.485**	**-0.479**	**-0.276**	0.285	0.523	0.504
Cold Day 3	-0.022	*-0.030*	-0.031	**-0.114**	**-0.379**	**-0.492**	**-0.489**	**-0.295**	0.269	0.522	0.517
Cold Day 4	-0.003	*-0.014*	-0.025	**-0.100**	**-0.289**	**-0.363**	**-0.343**	**-0.189**	0.199	0.365	0.343
Cold Day 5	0.010	*-0.006*	-0.011	**-0.089**	**-0.289**	**-0.384**	**-0.398**	**-0.248**	0.176	0.388	0.398
Cold Day 6	-0.024	*-0.031*	-0.019	**-0.066**	**-0.221**	**-0.310**	**-0.326**	**-0.198**	0.136	0.313	0.319

Table 3.5 The calculated difference in mean temperature of the signal and the upstream section for the 6 Hot and 6 Cold temperature profiles at a signal length analysis of 6m. The values in bold represent possible hyporheic discharge locations because the signal is colder than the upstream section for the 6 Hot profiles and warmer for the 6 Cold profiles.

	River Meter Associated with Signal Analysis (m)										
	320	321	322	323	324	325	326	327	328	329	330
Hot Day 1	-0.051	**-0.077**	**-0.121**	**-0.162**	**-0.179**	**-0.167**	**-0.132**	**-0.066**	0.026	0.107	0.165
Hot Day 2	-0.035	**-0.060**	**-0.099**	**-0.135**	**-0.156**	**-0.157**	**-0.132**	**-0.075**	0.006	0.090	0.165
Hot Day 3	-0.052	**-0.071**	**-0.099**	**-0.126**	**-0.145**	**-0.139**	**-0.105**	**-0.047**	0.026	0.094	0.153
Hot Day 4	-0.038	**-0.037**	**-0.043**	**-0.060**	**-0.072**	**-0.064**	**-0.046**	**-0.026**	0.003	0.041	0.076
Hot Day 5	-0.058	**-0.083**	**-0.127**	**-0.176**	**-0.200**	**-0.184**	**-0.137**	**-0.066**	0.029	0.125	0.195
Hot Day 6	-0.002	**-0.021**	**-0.047**	**-0.071**	**-0.086**	**-0.089**	**-0.075**	**-0.041**	0.011	0.058	0.089
Cold Day 1	0.006	**0.008**	**0.017**	**0.038**	**0.058**	**0.065**	**0.061**	**0.052**	0.031	-0.002	-0.030
Cold Day 2	0.034	**0.036**	**0.035**	**0.041**	**0.058**	**0.068**	**0.060**	**0.041**	0.020	-0.003	-0.028
Cold Day 3	0.014	**0.019**	**0.026**	**0.040**	**0.056**	**0.063**	**0.058**	**0.049**	0.035	0.018	0.002
Cold Day 4	-0.010	**0.003**	**0.014**	**0.026**	**0.045**	**0.059**	**0.064**	**0.066**	0.059	0.041	0.020
Cold Day 5	0.004	**0.025**	**0.042**	**0.052**	**0.063**	**0.076**	**0.076**	**0.057**	0.031	0.008	-0.013
Cold Day 6	0.043	**0.037**	**0.030**	**0.031**	**0.039**	**0.048**	**0.053**	**0.052**	0.041	0.020	-0.004

Table 3.6 The results of the z-test for the 6 Hot and 6 Cold temperature profiles at a signal length analysis of 2m for river meters 215-225. A value of 1 indicates the mean of the upstream section is different than the mean of the signal at a 99% significance level. The values in bolds are to highlight the six signal analyses that have significantly different means during all Hot and Cold periods.

	River Meter Associated with Signal Analysis (m)										
	215	216	217	218	219	220	221	222	223	224	225
Hot Day 1	0	0	0	0	**1**	**1**	**1**	**1**	**1**	**1**	0
Hot Day 2	0	0	0	0	**1**	**1**	**1**	**1**	**1**	**1**	0
Hot Day 3	0	0	0	0	**1**	**1**	**1**	**1**	**1**	**1**	0
Hot Day 4	0	0	0	1	**1**	**1**	**1**	**1**	**1**	**1**	0
Hot Day 5	0	0	0	0	**1**	**1**	**1**	**1**	**1**	**1**	1
Hot Day 6	0	0	0	0	**1**	**1**	**1**	**1**	**1**	**1**	0
Cold Day 1	0	0	0	0	**1**	**1**	**1**	**1**	**1**	**1**	0
Cold Day 2	0	0	0	0	**1**	**1**	**1**	**1**	**1**	**1**	0
Cold Day 3	0	0	0	0	**1**	**1**	**1**	**1**	**1**	**1**	0
Cold Day 4	0	0	0	0	**1**	**1**	**1**	**1**	**1**	**1**	0
Cold Day 5	0	0	0	0	**1**	**1**	**1**	**1**	**1**	**1**	0
Cold Day 6	0	0	0	0	**1**	**1**	**1**	**1**	**1**	**1**	0

Table 3.7 The results of the z-test for the 6 Hot and 6 Cold temperature profiles at a signal length analysis of 6m for river meters 320-330. A value of 1 indicates the mean of the upstream section is different than the mean of the signal at a 99% significance level. The values in bold are to highlight the three signal analyses that have significantly different means during all Hot and Cold periods.

	River Meter Associated with Signal Analysis (m)										
	320	321	322	323	324	325	326	327	328	329	330
Hot Day 1	1	1	1	1	**1**	**1**	**1**	1	0	1	1
Hot Day 2	0	1	1	1	**1**	**1**	**1**	1	0	1	1
Hot Day 3	1	1	1	1	**1**	**1**	**1**	1	0	1	1
Hot Day 4	1	0	1	1	**1**	**1**	**1**	0	0	1	1
Hot Day 5	1	1	1	1	**1**	**1**	**1**	1	0	1	1
Hot Day 6	0	0	1	1	**1**	**1**	**1**	1	0	1	1
Cold Day 1	0	0	0	1	**1**	**1**	**1**	1	0	0	0
Cold Day 2	0	0	0	1	**1**	**1**	**1**	1	0	0	0
Cold Day 3	0	0	0	1	**1**	**1**	**1**	1	0	0	0
Cold Day 4	0	0	0	0	**1**	**1**	**1**	1	1	1	0
Cold Day 5	0	0	1	1	**1**	**1**	**1**	1	0	0	0
Cold Day 6	1	1	0	0	**1**	**1**	**1**	1	1	0	0

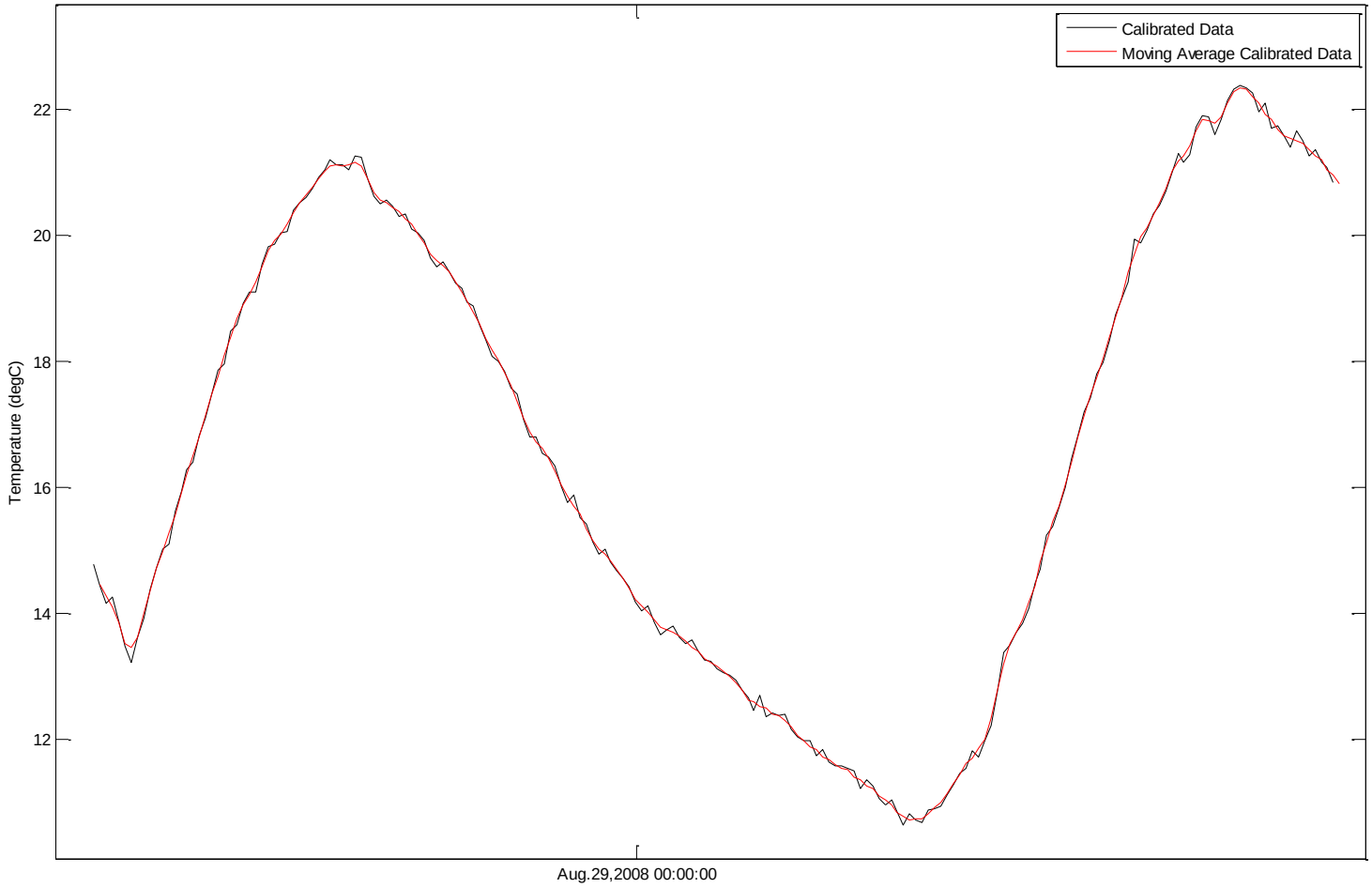
Calibrated Data
Moving Average Calibrated Data
Temperature (degC)
22
20
18
16
14
12
Aug.29,2008 00:00:00

Figure 3.4 Comparison of calibrated temperature data with 60 min-moving average calibrated temperature data for post-restoration river left cable. Applying the moving average minimizes the noise.

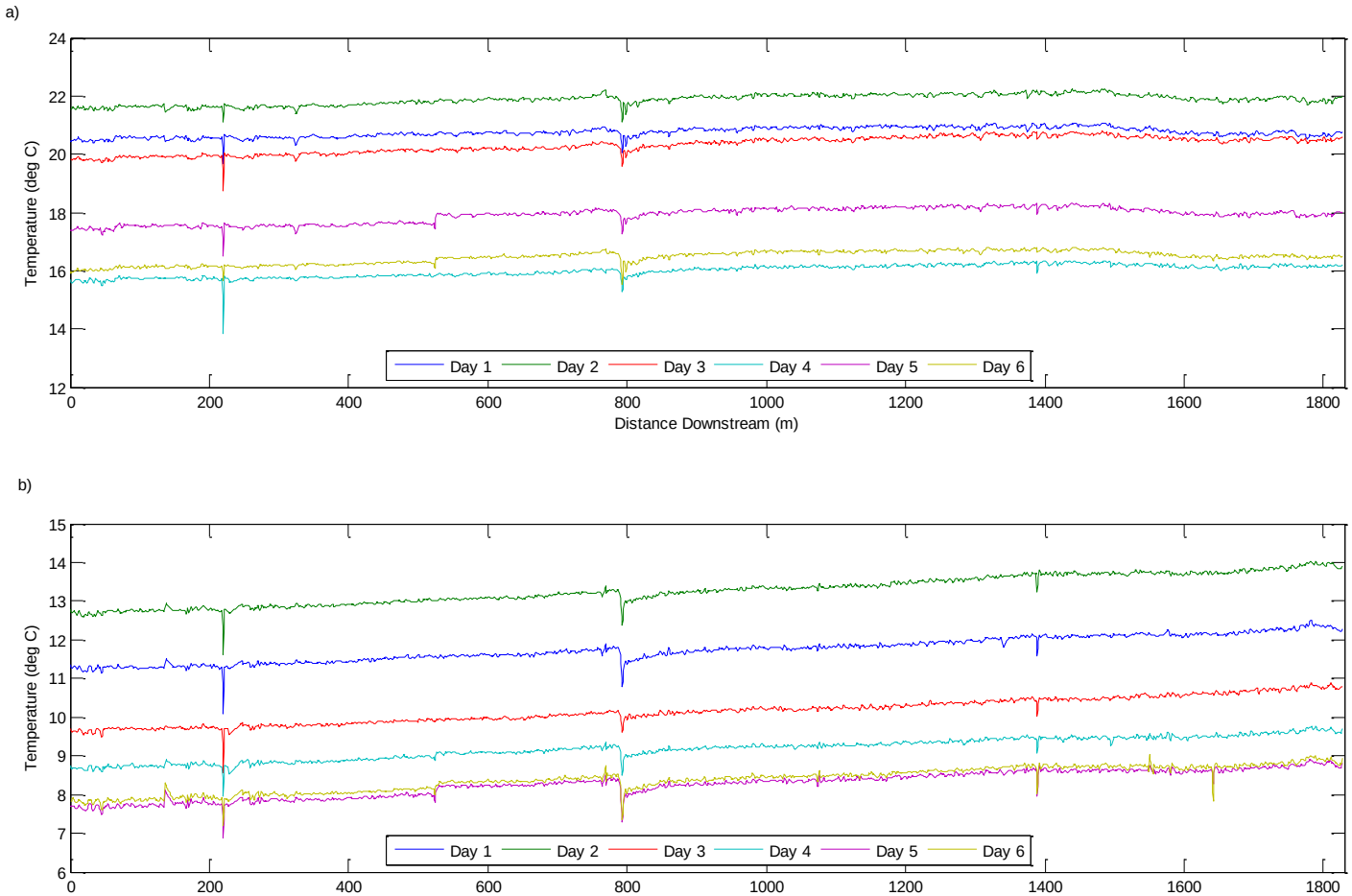

Figure 3.5 The profiles associated with the hottest 4 hours of the day a), “Hot” and coldest 4 hours of the day b) “Cold” for post-restoration river left cable.

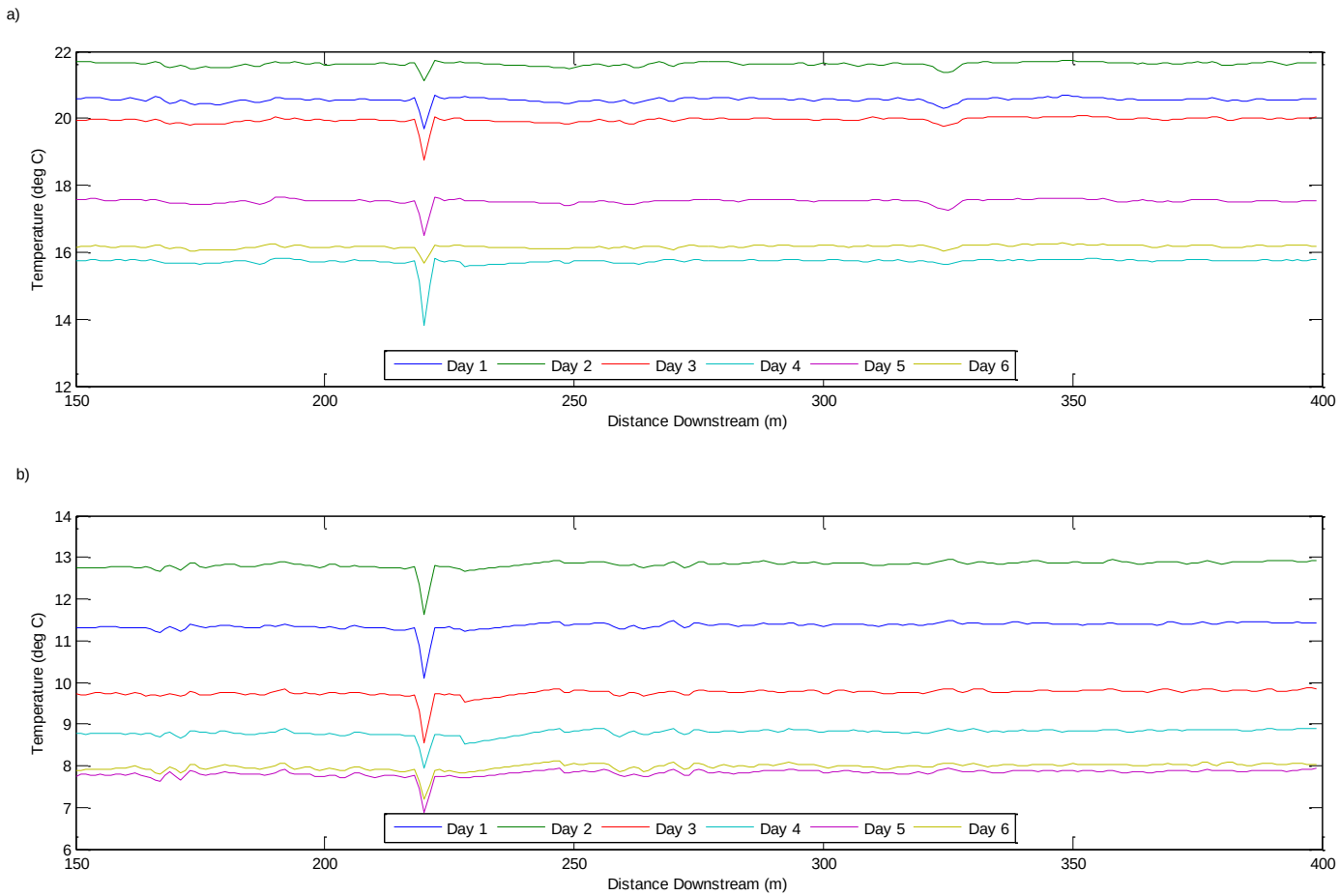

Figure 3.6 Hot, a), and Cold, b), profiles of river meter 205-225 and 315-335 which will be focused on for example calculations.

Next, the signals were separated into two groupings. The first is classified as groundwater inflow and includes all areas where the mean signal temperature is lower than the mean upstream temperature both for the Hot and Cold profiles. All 12 Hot and Cold temperature differences must pass the z-test at a 99% significance level to be considered groundwater inflow. The second group is classified as hyporheic discharge and is defined as areas where the mean signal temperature is cooler than the mean upstream temperature during for the Hot profiles but warmer than the mean upstream temperature for the Cold profiles. Again, all 12 profiles of Hot and Cold must pass this requirement to be considered hyporheic discharge.

For both of the groups, groundwater and hyporheic, there are multiple signal lengths strewn throughout the data that need to be discarded as artifacts of averaging. To eliminate the erroneous signals from the data, each 'cluster' of signal lengths was treated as having one true signal. There were six clusters in the groundwater group and seven clusters in the hyporheic group. There are two tributaries that enter the river within the study reach. The first, Davis creek, is a small creek whose confluence is at river meter 795. The second tributary is Vinegar creek and enters the MFJD at river meter 1505. Any cluster that overlaps with the confluence of these tributaries was disregarded as a valid signal.

To determine which signal length from the analysis is the correct signal length for each cluster, the sum of the absolute temperature difference was calculated. The calculated temperature difference is between the upstream and signal of the river at the respective signal length between 2-100m. The sum of the absolute temperature difference of meters 215-225 and 320-330 for the 11 different signal lengths can be found in Tables 3.8 and 3.9, respectively. The correct signal length corresponds to the largest sum of the absolute temperature difference for each cluster.

This analysis was performed on all four data sets, river left and river right of pre-restoration and river left and river right of post-restoration. Groundwater inflows were found in both of the post-restoration data sets but only in the river right pre-restoration data set. The lengths of groundwater inflows and the average change in temperature associated with the computed inflows are summarized in Table 3.10. Hyporheic flows were only found in the river left post-restoration data set and are summarized in Table 3.11.

Table 3.8 This table represents the sums of the absolute temperature difference for a signal analysis length of 2-100m. The absolute temperature difference was calculated using the temperatures associated with the signal and the section upstream with averaging lengths that correspond to the respective signal analysis (2-100m). The table represents river meters 215-225 which highlight a groundwater inflow at river meter 220 with a groundwater inflow length of 2m (in bold).

Length of Signal for Analysis (m)	River Meter Associated with Signal Analysis (m)										
	215	216	217	218	219	220	221	222	223	224	225
2	0.000	0.000	0.000	0.000	1.777	**8.075**	6.288	0.000	0.000	0.000	0.000
4	0.000	0.000	0.000	0.000	3.781	4.934	4.902	2.753	0.000	0.000	0.000
6	0.000	0.000	0.957	2.831	3.527	3.268	3.140	3.161	1.697	0.000	0.000
10	0.000	1.852	2.344	2.291	2.254	2.216	2.106	1.951	1.864	1.932	0.000
16	1.642	1.606	1.559	1.497	1.454	1.430	1.462	1.482	1.480	1.459	1.420
20	1.294	1.304	1.348	1.400	1.448	1.445	1.425	1.399	1.371	1.345	1.309
30	0.000	0.000	0.000	0.000	0.000	0.000	0.000	0.000	0.000	0.000	0.000
40	0.000	0.000	0.000	0.000	0.000	0.000	0.000	0.000	0.000	0.000	0.000
60	0.000	0.000	0.000	0.000	0.000	0.000	0.000	0.000	0.000	0.000	0.000
80	0.000	0.000	0.000	0.000	0.000	0.000	0.000	0.000	0.000	0.000	0.000
100	0.000	0.000	0.000	0.000	0.000	0.000	0.000	0.000	0.000	0.000	0.000

Table 3.9 This table represents the sums of the absolute temperature difference for a signal analysis length of 2-100m. The absolute temperature difference was calculated using the temperatures associated with the signal and the section upstream with averaging lengths that correspond to the respective signal analysis (2-100m). The table shows river meters 320-330 which highlights a hyporheic discharge at river meter 324 with a hyporheic discharge length of 6m (in bold).

Length of Signal for Analysis (m)	River Meter Associated with Signal Analysis (m)										
	320	321	322	323	324	325	326	327	328	329	330
2	0.000	0.000	0.000	0.000	0.000	0.000	0.000	0.000	0.000	0.000	0.000
4	0.000	0.000	0.000	0.000	0.498	0.387	0.000	0.000	0.000	0.000	0.000
6	0.000	0.000	0.000	0.000	**0.519**	0.423	0.256	0.000	0.000	0.000	0.000
10	0.000	0.000	0.000	0.000	0.000	0.300	0.216	0.107	0.000	0.000	0.000
16	0.000	0.000	0.000	0.000	0.000	0.000	0.000	0.000	0.000	0.000	0.000
20	0.000	0.000	0.000	0.000	0.000	0.000	0.000	0.000	0.000	0.000	0.000
30	0.000	0.000	0.000	0.000	0.000	0.000	0.000	0.000	0.000	0.000	0.000
40	0.000	0.000	0.000	0.000	0.000	0.000	0.000	0.000	0.000	0.000	0.000
60	0.000	0.000	0.000	0.000	0.000	0.000	0.000	0.000	0.000	0.000	0.000
80	0.000	0.000	0.000	0.000	0.000	0.000	0.000	0.000	0.000	0.000	0.000
100	0.000	0.000	0.000	0.000	0.000	0.000	0.000	0.000	0.000	0.000	0.000

Table 3.10 Results of the groundwater inflow analysis. Lengths and locations of the groundwater inflows are summarized along with the average temperature difference associated with the respective groundwater inflow.

Pre - Restoration				Post - Restoration			
River Left		River Right		River Left		River Right	
Areas of GW inflow (m)	Average ΔT (°C)	Areas of GW inflow (m)	Average ΔT (°C)	Areas of GW inflow (m)	Average ΔT (°C)	Areas of GW inflow (m)	Average ΔT (°C)
-	-	85-114	-0.046	32-35	-0.092	272-371	-0.040
-	-	588-667	-0.036	146-235	-0.037	-	-
-	-	-	-	219-220	-0.673	-	-
-	-	-	-	1585-1604	-0.057	-	-

Table 3.11 Results of the hyporheic discharge analysis. Lengths and locations of the hyporheic discharge are summarized along with the average absolute temperature difference associated with the respective hyporheic discharge location.

Pre - Restoration				Post - Restoration			
River Left		River Right		River Left		River Right	
Areas of HY discharge(m)	Average ΔT (°C)	Areas of HY discharge(m)	Average ΔT (°C)	Areas of HY discharge(m)	Average ΔT (°C)	Areas of HY discharge(m)	Average ΔT (°C)
-	-	-	-	162-171	0.072	-	-
-	-	-	-	321-326	0.097	-	-
-	-	-	-	1086-1105	0.031	-	-
-	-	-	-	1651-1730	0.047	-	-
-	-	-	-	1760-1779	0.075	-	-

Google Earth was used to visually compare the temperature signals with locations of ELJs. The groundwater inflows and hyporheic discharges were imported into Google Earth at the respective length for each signal. The ELJs were added specifying which bank they were installed on, see Figure 3.7. Before restoration occurred on this site, three locations of groundwater inflow were identified with two of the three signals occurring within the restoration boundaries. Once restoration was complete five groundwater inflows and five hyporheic discharge locations were discovered, with seven of these ten occurring within the boundaries of the restoration. From comparison of the Google Earth map, five of the post-restoration signals contained at least one ELJ.

To compare floodplain characteristics at the signal locations, LiDAR data were overlaid onto the groundwater and hyporheic results in Google Earth. The historic channels within the floodplain are clear in the LiDAR data and are in the same area as the downstream locations of groundwater and hyporheic, see Figure 3.8. The channel in this area has also been straightened by the historical railroad grade. The upstream locations do not have a distinct historical channel like the downstream locations and the river is more sinuous and not confined by the railroad grade, see Figure 3.9.

The locations of groundwater and hyporheic were identified in the photographs taken during documentation of the cable installation. These photographs allow a rudimentary look into the geomorphic controls of the signal, for example, the area of hyporheic discharge at river meters 1651-1730 is characterized as a riffle pool sequence seen in Figure 3.10. It is typical for geomorphic controls such as riffle-pool or pool-step sequences to be associated with hyporheic exchange (Bencala and Walters, 1983). Within the study site three of the five hyporheic discharge locations occur at riffle-pool sequences.

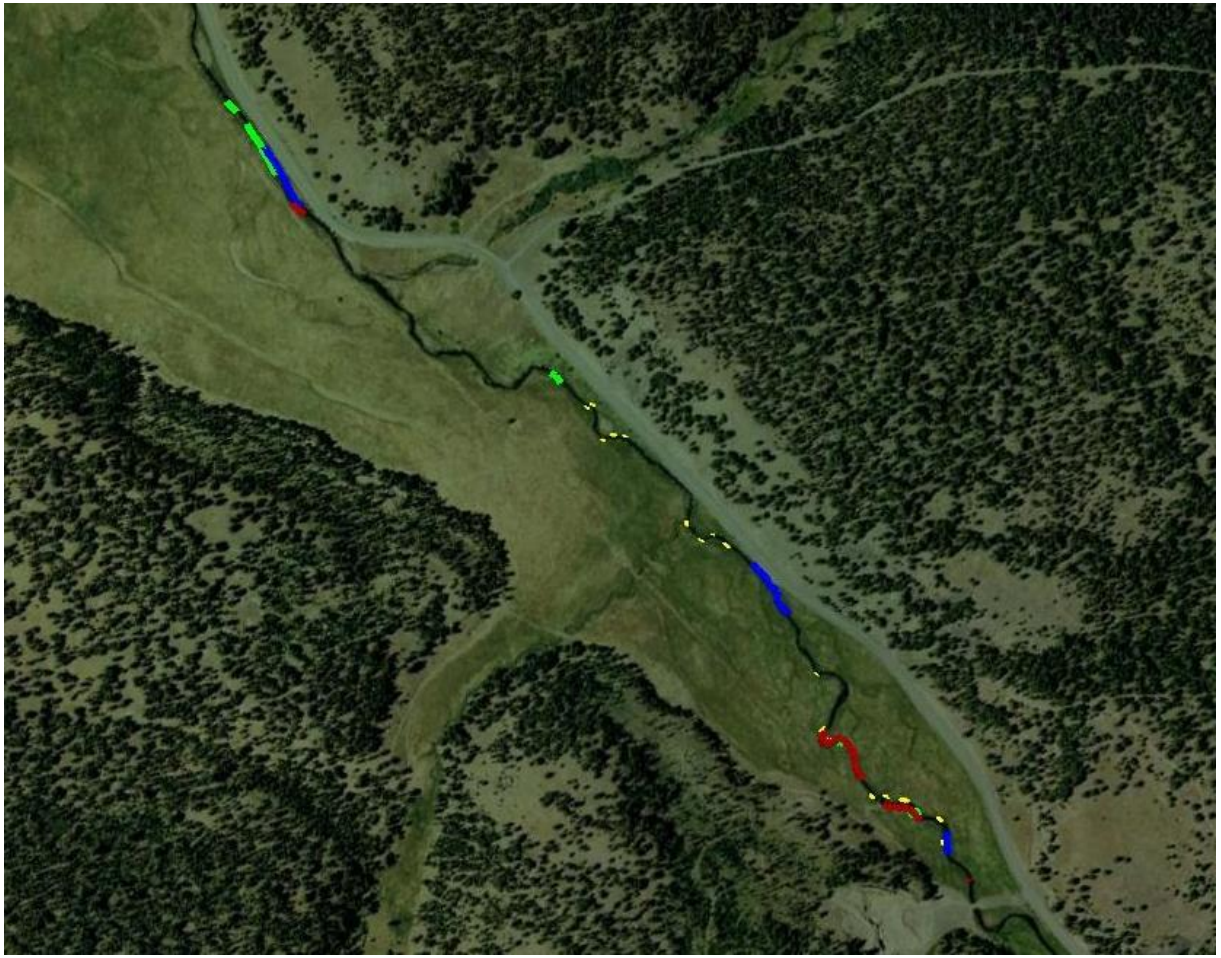

Figure 3.7 Google Earth image of the study site with the ELJs (yellow), the pre-restoration groundwater locations (blue) and the post-restoration groundwater locations (red) and hyporheic locations (green) (*Google Earth*, n.d.).

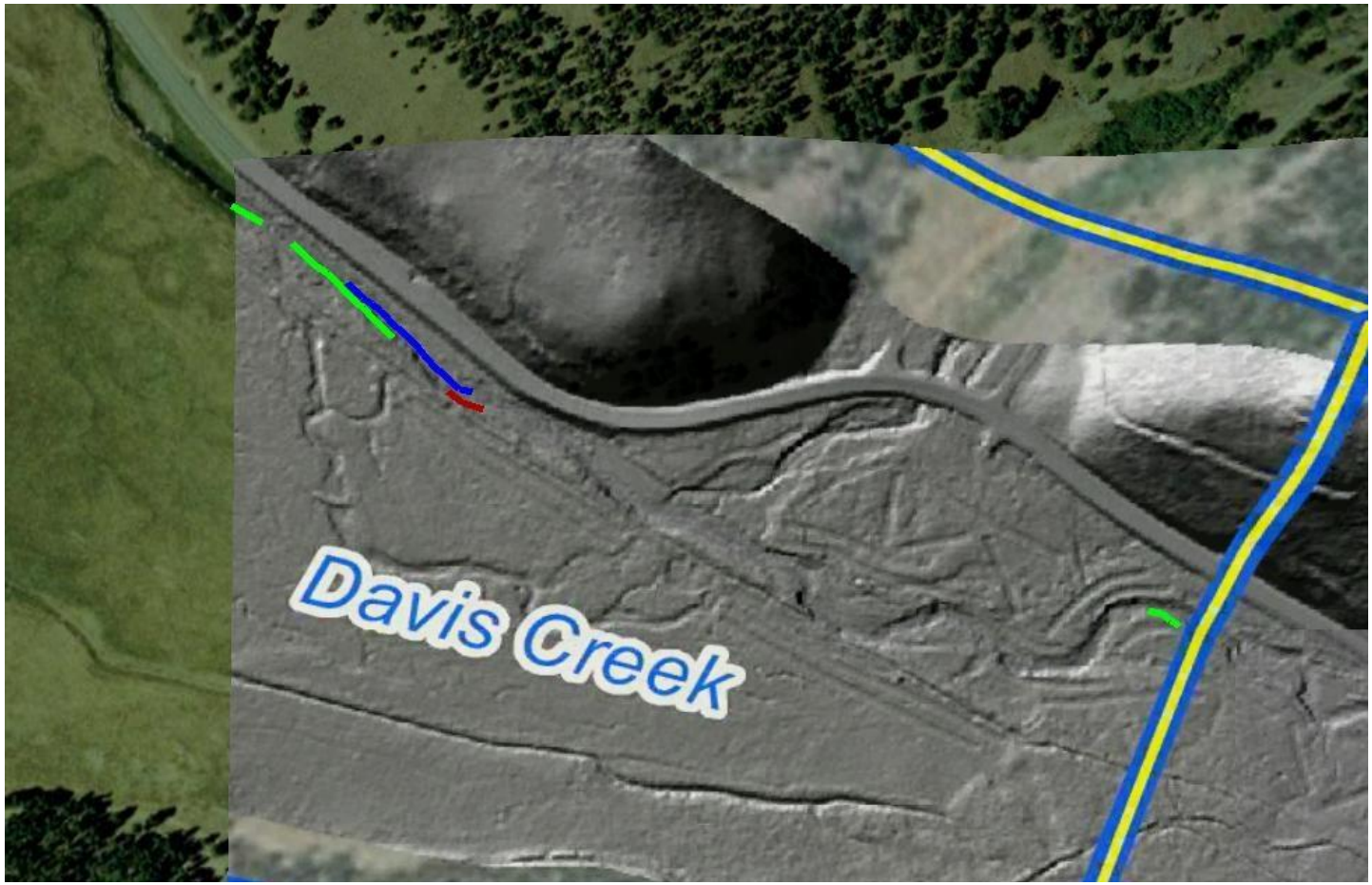

Figure 3.8 Google Earth image with the LiDAR data overlaid on the downstream half of the site. The pre-restoration groundwater locations (blue) and the post-restoration groundwater locations (red) and hyporheic locations (green) are highlighted (*Google Earth*, n.d.).

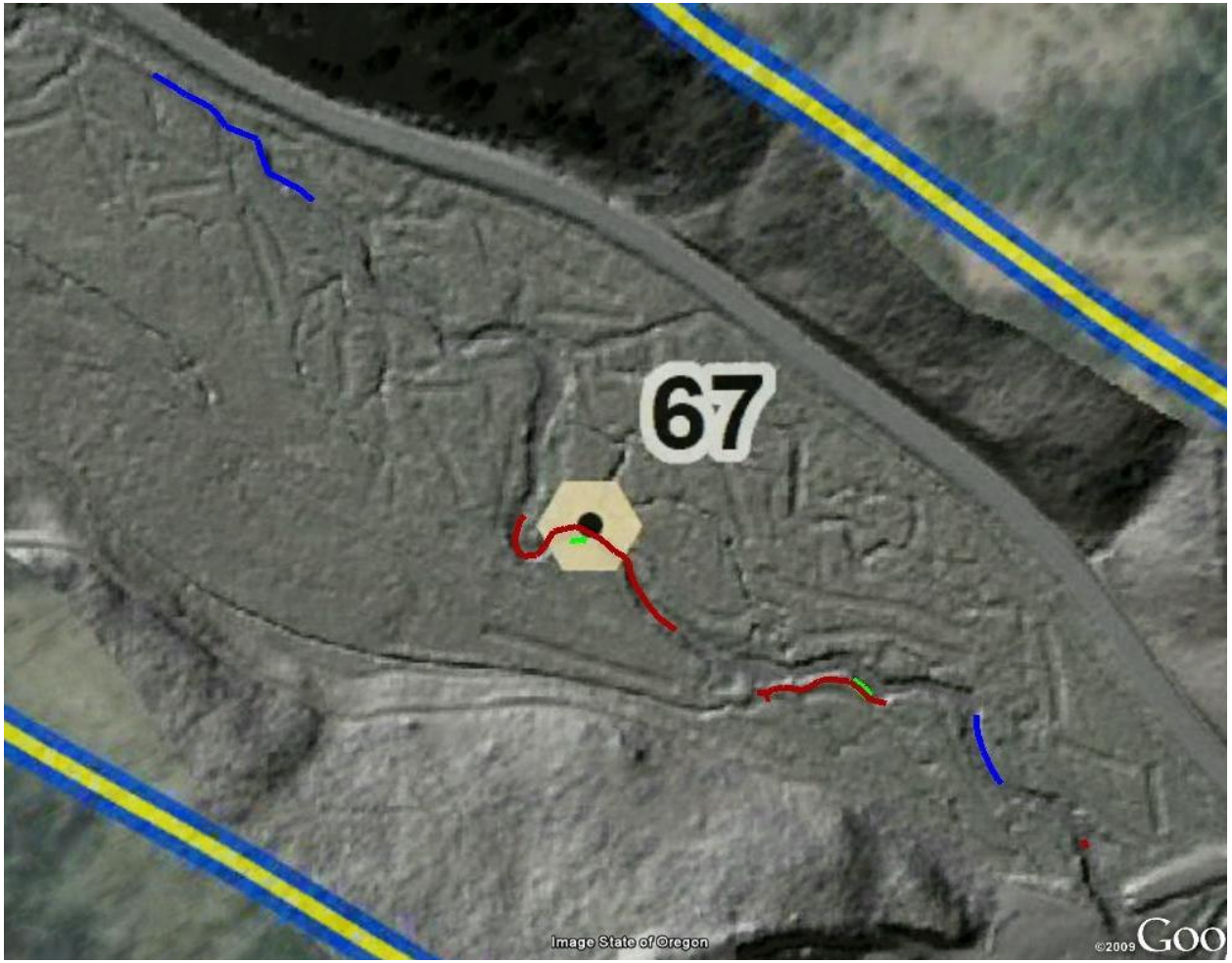

Figure 3.9 Google Earth image with the LiDAR data overlaid on the upstream half of the site. The pre-restoration groundwater locations (blue) and the post-restoration groundwater locations (red) and hyporheic locations (green) are highlighted (*Google Earth*, n.d.).

Figure 3.10 The location of a hyporheic discharge from post-restoration analysis, river meters 1086-1105. The meter on the whiteboard corresponds to the cable meter, not the river meter.

Groundwater Inflow Quantification

To determine how much groundwater inflow is occurring at each site, mass and energy conservation equations are used (see equations 3.3 and 3.4). The upstream flow and temperature as well as the groundwater and downstream temperature are needed to calculate the groundwater flow. The groundwater temperature is assumed to be constant at 6 °C, the mean annual air temperature. The upstream and downstream temperatures are taken from the DTS data described above. The upstream flow is calculated in Chapter 2: Field Measurements and Instrumentation for both pre-and post- restoration. The flow is not constant with time during the pre-restoration period. Therefore, the flow at the upstream boundary is linearly interpolated for the 10 days of groundwater analysis and the results can be found in Table 3.12. The flow is considered to be constant with time for the post-restoration study period with a flow of 0.340 m^3/s at the upstream boundary. For both the pre- and post-restoration analysis the flow increases downstream due to the two tributaries and the cumulative effect of the groundwater inflows. The flows used to calculate the groundwater inflows will incorporate both the tributaries and the upstream groundwater inflows.

At every groundwater inflow location, the flow is calculated for each Hot and Cold period for all analysis days. An example calculation of equation (3.5) for the groundwater inflow at river meters 219-220 of the Cold profile of river left post-restoration Day 1 is:

$$Q_g = 0.327\, m^3/s \left(\frac{11.284°\text{C} - 11.236°\text{C}}{11.236°\text{C} - 6.00°\text{C}}\right) = 0.003 m^3/s \qquad (3.6)$$

For pre-restoration, the 20 flows are then averaged and this averaged flow is the calculated groundwater inflow for each respective location. The post-restoration analysis uses only 6 days, therefore there are only 12 flows that are averaged for each groundwater inflow. The total flow added to the study site from groundwater was calculated as 0.004 m^3/s (0.14 cfs) for pre-restoration and 0.012 m^3/s (0.41 cfs) for post-restoration this equates to 1% and 4% of stream flow, respectively. Although it appears that groundwater increases with stream flow this could be an artifact of groundwater temperature signals being muted by high stream flows. The results can be seen in Table 3.13.

Table 3.12 Pre-restoration flows (m^3/s) for the upstream boundary of the Forrest Property used to calculate groundwater inflows.

Date	Flow (m^3/s)
6/25	0.96
6/26	0.93
6/27	0.90
6/28	0.87
6/29	0.84
6/30	0.81
7/1	0.78
7/2	0.74
7/3	0.71
7/4	0.68

Table 3.13 The quantity of groundwater entering the stream at each location for pre- and post-restoration.

Pre - Restoration						Post-Restoration					
River Left			River Right			River Left			River Right		
Areas of GW inflow (m)	Average Flow (m^3/s)	standard deviation	Areas of GW inflow (m)	Average Flow (m^3/s)	standard deviation	Areas of GW inflow (m)	Average Flow (m^3/s)	standard deviation	Areas of GW inflow (m)	Average Flow (m^3/s)	standard deviation
-	-	-	85-114	0.002	0.001	32-35	0.0002	0.001	272-371	0.002	0.003
-	-	-	588-667	0.002	0.002	146-235	0.005	0.006	-	-	-
-	-	-	-	-	-	219-220	0.004	0.005	-	-	-
-	-	-	-	-	-	1585-1604	0.0003	0.001	-	-	-

Discussion

River temperature is an important component of a healthy salmonid habitat and unfortunately many Oregon Rivers are above Total Maximum Daily Load (TMDL) levels (Brett, 1952; US EPA, 2006). The surface water cooling is controlled by shading from riparian vegetation, evaporative cooling, groundwater inflows and hyporheic exchange. Groundwater inflows and hyporheic exchange are the only two processes that create pockets of cool thermal refugia, an important characteristic for salmonid survival during peak summer temperatures (Torgersen et al., 1999). Restoration of the Forrest property consisted of the addition of ELJs primarily for juvenile salmonid protection from predators and high flows. The objective of this study is to see if the ELJs also created cool thermal refugia through analysis of the DTS temperature profile and determine what cooling processes can be identified with the DTS.

The only temperature signal that can be associated with the restoration effort is the groundwater inflow located at river meter 219-220. This cool thermal refuge is located in the scour pool of the ELJ that was installed during restoration. The other groundwater inflow and hyporheic discharge locations of post-restoration also occur at ELJs but cannot be directly attributed to ELJs like river meter 219-220. The work of Torgerson et al. (1999) has shown that the upper MFJD has many thermal refugia and heterogeneity but the DTS profiles do not support this conclusion. Unfortunately, during the study, the DTS was not running properly which resulted in higher measurement noise than usual. This increase in noise can lead to unidentified locations of cool thermal refugia. This could be the cause for conflicting conclusions between Torgerson et al. (1999) and our study. Other factors that could cause variability in temperature between pre- and post-restoration analysis are flow, tributary temperature and water table levels. Even with increased measurement noise, the DTS was able to detect groundwater and hyporheic locations within the Forrest property for pre- and post-restoration. Groundwater and hyporheic exchange created cool thermal refugia that collectively had a temperature 0.1°C and 1.2°C cooler than the main channel for pre-restoration by for post-restoration.

The current literature is inconclusive as to whether groundwater interactions change with discharge. Some studies have shown there is no change in hyporheic exchange from both low baseflow to high baseflow (Wondzell, 2006) and low baseflow to high flow (Hanrahan, 2008). Other studies state the hyporheic zone decreases with increasing flow (Legrand-Marcq and Laudelout, 1985) while the work of Morrice et al. (1997) exhibits increasing hyporheic with increasing discharge. A change in discharge effects not only hyporheic exchange but groundwater inflows. The detailed work of Käser et al. (2009) relates the water table and an increase with discharge to the quantity of groundwater inflow received by the river. The study demonstrates how groundwater inflow can both increase and decrease during higher discharge. The results of the groundwater inflow suggest that in our study site, groundwater inflow decreases with increasing discharge. Though seen in these data, any extension of this observation would be speculation and beyond the scope of the study. A separate study would be needed to describe the exact relationship between subsurface flow and surface flow.

Although it is difficult to draw strong conclusions on the restoration efforts due to variability in measurement noise, the DTS still gives an interesting perspective of the river. The groundwater inflows within the Forrest reach have very distinct characteristics. The inflow is

occurring either in a few meters or over tens of meters, demonstrating direct or diffuse groundwater inflow. Thermal refugia are more likely to occur from direct groundwater inflow because the temperature difference is concentrated in a smaller area than diffuse groundwater inflow.

The LiDAR data give important insight into the signal locations near the downstream boundary. The confluence of a distinct historic channel can be seen in the LiDAR data and is located where the lower four signals are. An historic channel is a common path for groundwater inflow and hyporheic exchange because of the increased porosity and hydraulic conductivity of the material (Stanford and Ward, 1993). Therefore, the lower four groundwater and hyporheic locations are thought to be a result of the historic channel.

Our study shows that DTS can be a useful design tool for river restoration. With knowledge of direct and diffuse groundwater locations, scour pools and log structures can be placed appropriately to create cool thermal refugia. Structures can be placed with knowledge of thermal characteristics and not just flow characteristics. In addition, the DTS can identify locations of hyporheic exchange ensuring that these locations are not disturbed with restoration activities.

Appendix 3 References and additional useful citations

Allen, D., Dietrich, W., Baker, P., Ligon, F., & Orr, B. (2007). Development of a mechanistically based, basin-scale stream temperature model: applications to cumulative effects modeling. *USDA Forest Service Gen. Tech. Rep. PSW-GTR-194*, 11-24.

Anderson, M. P. (2005). Heat as a ground water tracer. *Ground Water*, *43*(6), 951-968.

Arrigoni, A. S., Poole, G. C., Mertes, L. A., O'Daniel, S. J., Woessner, W. W., & Thomas, S. A. (2008). Buffered, lagged, or cooled? Disentangling hyporheic influences on temperature cycles in stream channels. *Water Resources Research*, *44*(9), W09418.

Bartholow, J. (1999). SSTEMP for windows: the stream segment temperature model (Version 1.1.3). *US Geological Survey*, *29*. Retrieved from http://www.mesc.usgs.gov/rsm/rsm_download.html#TEMP

Baxter, C., Hauer, F. R., & Woessner, W. W. (2003). Measuring Groundwater–Stream Water Exchange: New Techniques for Installing Minipiezometers and Estimating Hydraulic Conductivity. *Transactions of the American Fisheries Society*, *132*(3), 493-502.

Bencala, K. E. (2005). Hyporheic exchange flows. *Encyclopedia of Hydrological Sciences*, *3*(Part 10), 1733–1740.

Bencala, K. E., & Walters, R. A. (1983). Simulation of Solute Transport in a Mountain Pool-and-Riffle Stream: A Transient Storage Model. *Water Resources Research*, *19*(3), 718-724.

Bernhardt, E. S., Palmer, M. A., Allan, J. D., Alexander, G., Barnas, K., Brooks, S., et al. (2005). *ECOLOGY: Synthesizing US River Restoration Efforts* (Vol. 308).

Beschta, R. L., & Ripple, W. J. (2005). Rapid assessment of riparian cottonwood recruitment: Middle Fork John Day River, Northeastern Oregon. *Ecological Restoration*, *23*(3), 150-156.

Boyd, M., & Kasper, B. (2004). Analytical methods for dynamic open channel heat and mass transfer: methodology for Heat Source Model Version 7.0. Retrieved from http://www.deq.state.or.us/WQ/TMDLs/tools.htm

Brett, J. R. (1952). Temperature tolerance in young Pacific salmon, genus Oncorhynchus. *Journal of the Fisheries Research Board of Canada*, *9*(6), 265–323.

Brett, J. R. (1956). Some principles in the thermal requirements of fishes. *The Quarterly Review*

of Biology, *31*(2), 75-87.
Caissie, D. (2006). The thermal regime of rivers: a review. *Freshwater Biology*, *51*(8), 1389–1406.
Collier, M. W. (2008). *Demonstration of fiber optic distributed temperature sensing to differentiate cold water refuge between ground water inflows and hyporheic exchange* (MA Thesis). Oregon State University. Retrieved from Google Scholar.
Conant, B. (2004). Delineating and quantifying ground water discharge zones using streambed temperatures. *Ground Water*, *42*(2), 243-257.
Cox, M., & Bolte, J. (2007). A spatially explicit network-based model for estimating stream temperature distribution. *Environmental Modelling & Software*, *22*(4), 502-514. doi: 10.1016/j.envsoft.2006.02.011
Crispell, J. K., Endreny, T. A., & Foundation, E. B. (2009). Hyporheic exchange flow around constructed in-channel structures and implications for restoration design. *Hydrological Processes*, *23*(8), 1158–1168.
Evans, E. C., McGregor, G. R., & Petts, G. E. (1998). River energy budgets with special reference to river bed processes. *Hydrological Processes*, *12*(4), 575-595.
Fernald, A. G., Landers, D. H., & Wigington Jr, P. J. (2006). Water quality changes in hyporheic flow paths between a large gravel bed river and off-channel alcoves in Oregon, USA. *River Research and Applications*, *22*(10), 1111–1124.
Fernald, A. G., Wigington, P. J., & Landers, D. H. (2001). Transient storage and hyporheic flow along the Willamette River, Oregon: Field measurements and model estimates. *Water Resources Research*, *37*(6), 1681-1694.
Findlay, S. (1995). Importance of surface-subsurface exchange in stream ecosystems: The hyporheic zone. *Limnology and Oceanography*, *40*(1), 159-164.
Google Earth. (n.d.). . Google.
Gooseff, M. N., Anderson, J. K., Wondzell, S. M., LaNier, J., & Haggerty, R. (2006). A modelling study of hyporheic exchange pattern and the sequence, size, and spacing of stream bedforms in mountain stream networks, Oregon, USA. *Hydrological Processes*, *20*(11), 2443–2457.
Gooseff, M. N., Wondzell, S. M., Haggerty, R., & Anderson, J. (2003). Comparing transient storage modeling and residence time distribution (RTD) analysis in geomorphically varied reaches in the Lookout Creek basin, Oregon, USA. *Advances in Water Resources*, *26*(9), 925-937.
Hanrahan, T. P. (2008). Effects of river discharge on hyporheic exchange flows in salmon spawning areas of a large gravel-bed river. *Hydrological Processes*, *22*(1), 127-141. doi: 10.1002/hyp.6605
Harvey, J. W., & Wagner, B. J. (2000). Quantifying hydrologic interactions between streams and their subsurface hyporheic zones. *Streams and Ground Waters*, 3–44.
Hester, E. T., Doyle, M. W., & Poole, G. C. (2009). The influence of in-stream structures on summer water temperatures via induced hyporheic exchange. *Limnology and Oceanography*, *54*(1), 355–367.
Hester, E. T., & Doyle, M. W. (2008). In-stream geomorphic structures as drivers of hyporheic exchange. Retrieved from http://www.agu.org.proxy.library.oregonstate.edu/pubs/crossref/2008/2006WR005810.shtml
Hypothesis Test Assumptions. (2009). *The MathWorks*. Retrieved September 16, 2009, from

http://www.mathworks.com/access/helpdesk/help/toolbox/stats/f13914.html
Independent Scientific Advisory Board. (2003). A review of strategies for recovering tributary habitat. *Northwest Power and Conservation Council. ISAB*, *2*.
Johnson, S. L. (2003). Stream temperature: scaling of observations and issues for modelling. *Hydrological Processes*, *17*(2), 497–499.
Kasahara, T., & Hill, A. R. (2008). Modeling the effects of lowland stream restoration projects on stream–subsurface water exchange. *Ecological Engineering*, *32*(4), 310-319.
Kobayashi, D. (1985). Separation of the snowmelt hydrograph by stream temperatures. *Journal of Hydrology*, *76*, 155-165.
Kulongoski, J. T., & Izbicki, J. A. (2008). Simulation of fluid, heat transport to estimate desert stream infiltration. *Ground Water*, *46*(3), 462-474.
Lacey, R. W., & Millar, R. G. (2004). Reach scalye hydraulic assessment of instream salmonid habitat restoration. *Journal of the American Water Resources Association*, *40*(6), 1631–1644.
Legrand-Marcq, C., & Laudelout, H. (1985). Longitudinal dispersion in a forest stream. *Journal of Hydrology*, *78*(3-4), 317-324. doi: 10.1016/0022-1694(85)90109-X
Loheide II, S. P., & Gorelick, S. M. (2006). Quantifying stream-aquifer interactions through the analysis of remotely sensed thermographic profiles and in situ temperature histories. *Environ. Sci. Technol*, *40*, 3336-3341.
Lowry, C. S., Walker, J. F., Hunt, R. J., & Anderson, M. P. (2007). Identifying spatial/variability of groundwater discharge in a wetland stream using a distributed temperature sensor. *Water Resources Research*, *43*(10), 10408.
McCullough, D. A. (1999). *A review and synthesis of effects of alterations to the water temperature regime on freshwater life stages of salmonids, with special reference to chinook salmon* (Project Report). Seattle, WA: U.S. Environmental Protection Agency.
McDonald, L. L., Bilby, R., Bisson, P. A., Coutant, C. C., Epifanio, J. M., Goodman, D., et al. (2007). Research, monitoring, and evaluation of fish and wildlife restoration projects in the Columbia River Basin: lessons learned and suggestions for large-scale monitoring programs. *Fisheries*, *32*(12), 582–590.
Morrice, J., Valett, H., Dahm, C., & Cam, M. (1997). Alluvial Characteristics, Groundwater-Surface Water Exchange and Hydrological Retention in Headwater Streams. *Hydrological Processes*, *11*(3), 253-267. doi: 10.1002/(SICI)1099-1085(19970315)11:3<253::AID-HYP439>3.0.CO;2-J
Neilson, B. T., Stevens, D. K., Chapra, S. C., & Bandaragoda, C. (2009). Data collection methodology for dynamic temperature model testing and corroboration. *Hydrological Processes*, *23*(20).
NOAA. (2009). Pacific Coastal Salmon Recovery Fund Data Website. *Pacific Coastal Salmon Recovery Fund*. Retrieved from http://webapps.nwfsc.noaa.gov/portal/page?_pageid=34,1&_dad=portal&_schema=PORTAL
Pacific Northwest Aquatic Monitoring Partnership. (2005, April 5). Establishing a network of intensively monitored watersheds in the Pacific Northwest.
Palmer, M. A., Bernhardt, E. S., Allan, J. D., Lake, P. S., Alexander, G., Brooks, S., et al. (2005). Standards for ecologically successful river restoration. *Journal of Applied Ecology*, *42*(2), 208-217. doi: 10.1111/j.1365-2664.2005.01004.x
Poole, G. C., O'Daniel, S. J., Jones, K. L., Woessner, W. W., Bernhardt, E. S., Helton, A. M., et

al. (2008). Hydrologic spiralling: the role of multiple interactive flow paths in stream ecosystems. *Regulated Rivers: Research & Management*, *24*(7), 1018–1031.

Poole, G. C., & Berman, C. H. (2001). An ecological perspective on in-stream temperature: natural heat dynamics and mechanisms of human-caused thermal degradation. *Enviromental Management*, *27*(6), 787-802.

Roth, T. R., Selker, J. S., Westhoff, M. C., Gabrielli, J., Huwald, H., & Parlange, M. (2008). Small scale stream restoration simulation and response on stream temperature using a physically based temperature model. In *2008 Joint Meeting of The Geological Society of America*.

Roth, T., Westhoff, M., Huwald, H., Huff, J., Rubin, J., Barrenetxea, G., et al. (2010). Stream Temperature Response to Three Riparian Vegetation Scenarios Using a Distributed Temperature Validated Model. *Environ. Sci. and Tech.*

Runkel, R. L. (1998). One-dimensional transport with inflow and storage (OTIS): a solute transport model for streams and rivers. *US Geological Survey Water-Resources Investigation Report*, *98*, 4018.

Runkel, R. L., McKnight, D. M., & Rajaram, H. (2003). Modeling hyporheic zone processes. *Advances in Water Resources*, *26*(9), 901-905.

Selker, J., van de Giesen, N., Westhoff, M., Luxemburg, W., & Parlange, M. B. (2006). Fiber optics opens window on stream dynamics. *Geophys. Res. Lett*, *33*(24), 24401.

Selker, J. S., Selker, J., Gabrielli, J., Gregory, C., Saydec, C., Tufillaro, N., et al. (2008). Taking the temperature of ecological systems with fiber optics. *Eos Trans. AGU*, *89*(20), 187.

Selker, J. S., Thévenaz, L., Huwald, H., Mallet, A., Luxemburg, W., Van de Giesen, N., et al. (2006). Distributed fiber-optic temperature sensing for hydrologic systems. *Water Resour. Res*, *42*, W12202.

Silliman, S. E., & Booth, D. F. (1993). Analysis of time-series measurements of sediment temperature for identification of gaining vs. losing portions of Juday Creek, Indiana. *Journal of Hydrology*, *146*, 131-148. doi: 10.1016/0022-1694(93)90273-C

Sinokrot, B. A., & Stefan, H. G. (1993). Stream temperature dynamics: measurements and modeling. *Water Resources Research*, *29*(7), 2299-2312.

Smith, C. (1998). Pacific Northwest Salmon History Snapshots. Retrieved October 19, 2009, from http://oregonstate.edu/instruct/anth481/fish.html

Stanford, J. A., & Ward, J. V. (1993). An ecosystem perspective of alluvial rivers: connectivity and the hyporheic corridor. *Journal of the North American Benthological Society*, 48–60.

Taylor, S. B. (2007). Watershed assessment, river restoration, and the geoscience profession in Oregon. *Oregon Geology*, *68*(1), 27.

Torgersen, C. E., Faux, R. N., McIntosh, B. A., Poage, N. J., & Norton, D. J. (2001). Airborne thermal remote sensing for water temperature assessment in rivers and streams. *Remote Sensing of Environment*, *76*(3), 386-398.

Torgersen, C. E., Price, D. M., Li, H. W., & McIntosh, B. A. (1999). Multiscale thermal refugia and stream habitat associations of Chinook salmon in Northeastern Oregon. *Ecological Applications*, *9*(1), 301-319.

Tufillaro, N., Dorighi, J., Collier, M., & Selker, J. (2008). Measuring Stream Dynamics with Fiber Optics. In *American Physical Society, 10th Annual Meeting of the Northwest Section of APS, May 15-17, 2008, abstract# G3. 001*.

Turo, S. (2009, February). *Habitat Restoration within the Ceded lands of The Confederated Tribes of the Warm Springs Reservation of Oregon*. Presented at the River Restoration

NW, Power Point, Skamania Lodge, WA.
Tyler, S. W., Selker, J. S., Hausner, M. B., Hatch, C. E., Torgersen, T., Thodal, C. E., et al. (2009). Environmental temperature sensing using Raman spectra DTS fiber-optic methods. *Water Resources Research*, *45*(null).
US EPA. (2006). 2006 Section 303(d) List Fact Sheet for OREGON | WATERS | US EPA. Retrieved July 1, 2009, from http://oaspub.epa.gov/tmdl/state_rept.control?p_state=OR&p_cycle=2006
Westhoff, M. C., Savenije, H. H. G., Luxemburg, W. M. J., Stelling, G. S., van de Giesen, N. C., Selker, J. S., et al. (2007). A distributed stream temperature model using high resolution temperature observations. *Hydrology and Earth System Sciences*, *11*(4), 1469.
Wohl, E., Angermeier, P. L., Bledsoe, B., Kondolf, G. M., MacDonnell, L., Merritt, D. M., et al. (2005). River restoration. *Water Resources Research*, *41*(10), W10301.
Wondzell, S. M. (2006). Effect of morphology and discharge on hyporheic exchange flows in two small streams in the Cascade Mountains of Oregon, USA. *Hydrological Processes*, *20*(2), 267–287.
Wondzell, S. M., Gooseff, M. N., & McGlynn, B. L. (2007). Flow velocity and the hydrologic behavior of streams during baseflow. *Geophysical Research Letters*, *34*(24), L24404.
Wondzell, S. M., & Swanson, F. J. (1996). Seasonal and Storm Dynamics of the Hyporheic Zone of a 4th-Order Mountain Stream. II: Nitrogen Cycling. *Journal of the North American Benthological Society*, *15*(1), 20-34.